



CHALMERS
UNIVERSITY OF TECHNOLOGY



The outflow of the Boomerang Nebula

The coldest object in the Universe
MSc thesis in Physics and Astronomy

JUSTIN SALÉR-RAMBERG

MASTER'S THESIS 2016:NN

The outflow of the Boomerang Nebula

The coldest object in the Universe

JUSTIN SALÉR-RAMBERG



CHALMERS
UNIVERSITY OF TECHNOLOGY

Department of Earth and Space Science
Radio Astronomy and Astrophysics
CHALMERS UNIVERSITY OF TECHNOLOGY
Gothenburg, Sweden 2016

The outflow of the Boomerang Nebula
The coldest object in the Universe
JUSTIN SALÉR-RAMBERG

© JUSTIN SALÉR-RAMBERG, 2016.

Supervisors: Wouter Vlemmings and Theo Khouri, Department of Earth and Space
Sciences

Examiner: Wouter Vlemmings, Department of Earth and Space Sciences

Master's Thesis 2016:NN
Department of Earth and Space Sciences
Radio Astronomy and Astrophysics
Chalmers University of Technology
SE-412 96 Gothenburg
Telephone +46 31 772 1000

Cover: An image of the Boomerang Nebula taken by the Hubble Space Telescope

Typeset in L^AT_EX
Printed by [Name of printing company]
Gothenburg, Sweden 2016

The Outflow of the Boomerang Nebula
The coldest object in the Universe
JUSTIN SALÉR-RAMBERG
Department of Earth and Space Sciences
Chalmers University of Technology

Abstract

The Boomerang Nebula is a preplanetary nebula with a massive and fast outflow. The gas in the outflow is seen as absorption against the cosmic microwave background, making it the coldest known naturally occurring object in the Universe. Like an interstellar refrigerator, the outflow cools itself adiabatically. Old observations with Swedish-ESO Submillimetre Telescope (SEST) were consistent with a constant-velocity outflow, but more recent observations, with Atacama Large Millimeter/submillimeter Array (ALMA), pointed to a model with an outflow velocity which varies radially. This thesis aims to reproduce the ALMA observations by considering two different scenarios, a scenario with an explosive event in which the material was ejected with a range of velocities and a scenario with an outflow with a time variable expansion velocity. The best-fit models for both scenarios produce similar spectra on the large scale, as the Boomerang Nebula in a larger region, but have difficulties matching the spectra along the line of sight through the center of the shell. The models that fit the data the best are similar to each other. The thesis also shows a model with a larger shell size than observed, that provides a good fit to the observations. While it is outside the scope of this thesis, it serves as a clue for future analysis of the Boomerang Nebula.

Keywords: Stellar Physics, Astronomy, Stellar Winds, Outflow, Preplanetary Nebula

Acknowledgements

First of all, I want to thank my supervisors Wouter Vlemmings and Theo Khouri who have dedicated a lot of time and effort to guide me along my thesis. They have had to answer to a lot of stupid questions and listen to a lot of stupid ideas. I want to thank them for not giving up and kept supporting me until the very end. Without their unwavering support this thesis would not have been possible. I want to thank the rest of the Star Formation and Evolved Star group for welcoming me into their circle and teaching me a lot about the field.

I want to thank Ivan Marti-Vidal for a crash course in CASA python scripts. I want to thank the rest of the staff at Onsala Space Observatory for being among the most friendly, curious and dedicated people I have ever had the chance to meet. I am really grateful for the chance to spend half a year with you. I also want to thank my family for always supporting me. And most of all I want to thank my other half, Wenzhao Liu, for forcing me to work and helping me to relax. Justin

Salér-Ramberg, Gothenburg, August 2016

Contents

1	Introduction	1
1.1	Units	2
1.2	Star formation and the main sequence	3
1.3	Red giant branch and asymptotic giant branch	5
1.4	Planetary nebulae	5
1.5	Stellar effects on the ISM	6
1.6	Boomerang Nebula	7
1.7	Probing the circumstellar environment	8
1.8	Telescopes	10
2	Stellar Winds	11
2.1	Heating and cooling processes	12
2.2	Photodissociation	13
3	Motivation and methods	15
3.1	Outflow simulations	18
3.1.1	Explosion scenario	18
3.1.2	Decreasing velocity scenario	19
3.1.3	Temperature profile	19
3.2	Radiative transfer	19
4	Results	23
4.1	Explosion scenario	24
4.2	Decreasing velocity scenario	31
4.3	Considering a large shell size	34
5	Conclusion	39
5.1	Interpretation of Results	39
5.2	Wind mechanism	39
6	Future Prospects	43
	Bibliography	45

List of Figures

1.1	A Hertzsprung Russel diagram showing the relationship between the luminosity and the temperature of a star. This plot clearly shows the main sequence full of young stars. The central star of the Boomerang Nebula is a post-AGB star. It has just left the AGB branch and is on it's way to become a white dwarf. [1]	4
1.2	A schematic view of the AGB star during thermal pulses. Hydrogen burning happens in the envelope of the star producing helium. When enough helium has been created, helium burning is reignited pushing out the hydrogen envelope.	6
1.3	A schematic view of the Boomerang Nebula and its shell. The focus of this thesis is the Nebula's absorbing outer shell, the coldest known naturally occurring object in the Universe.	8
3.1	The spectra of the CO($J = 1 - 0$) line from the SEST+ALMA data, given at four different apertures. The spectrum in the upper-left panel is similar to the SEST spectrum, while the spectrum in the lower-right panel was obtained from a much smaller aperture.	16
3.2	The first upper-left panel shows the CO($J = 1 - 0$) line from a large aperture around the Boomerang Nebula. It is included to show how the original SEST data looked like. From the spectrum, it is hard to say anything about the velocity's radial behavior. In the center of the line, there is emission from the inner shell. The upper-right panel shows the same line for a constant velocity model, to show that it is possible to describe the SEST data with it. The lower-left panel shows the CO line extracted from the ALMA data using an aperture smaller than the shell. The lower-right panel shows how a constant velocity model would look in the same aperture. A constant velocity model is not able to describe the ALMA spectrum and, hence, a model with a radially dependent velocity profile is required.	17
3.3	How the simulation determined if two mass bins collided. The particles had positions r_i and r_j and velocities v_i and v_j respectively.	18
4.1	The logarithm of the density for an explosion model. The explosion used the parameters $v_c = 120$ km/s and $v_o = 100$ km/s (see Equation (3.3)). The total gas mass is $M = 2.9M_\odot$. The model includes an AGB wind moving at a velocity of 15 km/s and has a mass loss rate of $\dot{M} \approx 10^{-5}M_\odot/\text{year}$	24

4.2	The temperature profile for an explosive wind colliding with an AGB wind. The explosion uses the parameters $v_c = 120\text{km/s}$ and $v_o = 100\text{ km/s}$ (see Equation (3.3)) and the total gas mass is $1.4M_\odot$. The AGB wind has a velocity at 15 km/s and a mass loss rate rate of $\dot{M} \approx 10^{-5}M_\odot/\text{year}$	25
4.3	Spectra for an explosion scenario model with an AGB wind, at different times. The explosion model has parameters $v_c = 120\text{ km/s}$ and $v_o = 100\text{ km/s}$ (see Equation (3.3)) and a total mass of $2.9M_\odot$. The AGB wind is moving at a constant velocity of 15 km/s and had a mass loss rate of $10^{-5}M_\odot/\text{year}$. After 1150 years, the AGB wind has left the shell.	25
4.4	The Gaussian distribution of an explosion with $v_c = 120\text{ km/s}$ and $v_o = 40\text{ km/s}$. The velocity at the outer edge of the cold shell is $v_{out} = v_c + 2v_o$ and the velocity at it's inner edge is v_{in} . At this time, most of the mass from the explosion is inside the shell.	26
4.5	The density profile for different parameters in the explosion scenario. The time is chosen accordingly to Equation (4.1). The profiles are compared to $\rho \propto r^{-2}$, the density profile for a constant wind velocity.	27
4.6	The temperature profile for different velocity parameters, v_o and v_c , in the explosion model. The time is chosen accordingly to Equation (4.1). The temperature asymptotes $T \propto r^{-4/3}$, the case of constant velocity without molecular heating, as the outflow velocity increases and the photoelectric heating weakens.	27
4.7	The absolute value of the different heating and cooling mechanisms in the explosion scenario, 1040 years after the initial explosion. The parameters $v_c = 100\text{ km/s}$ and $v_o = 60\text{ km/s}$, see Equation (3.3).The total gas mass in the explosion is $1.4M_\odot$	28
4.8	The intensity map of an outflow with the explosion scenario, 1150 years after the initial explosion. The parameters $v_c = 220\text{ km/s}$ and $v_o = 120\text{km/s}$, see Equation (3.3).The total gas mass in the explosion is $2.9M_\odot$. The color map is for velocities at $v = 0.5\text{ km/s}$	28
4.9	Spectra from the explosion scenario, for different values of v_c . The total gas mass is $M = 2.9M_\odot$. The offset velocity is $v_o = 100\text{ km/s}$	29
4.10	Spectra from the explosion scenario for different values of v_c . The total gas mass is $M = 2.9M_\odot$. The offset velocity is $v_o = 40\text{ km/s}$	29
4.11	Spectra from the explosion scenario for different values of v_o . The total gas mass is $M = 2.9M_\odot$. The central velocity is $v_c = 120\text{ km/s}$	30
4.12	Spectra from the explosion scenario for different gas mass M . The central velocity is $v_c = 120\text{ km/s}$ and the offset velocity is $v_o = 100\text{ km/s}$	30
4.13	The best fit of the explosion scenario to the SEST+ALMA data. This model has $v_c = 120\text{ km/s}$, $v_o = 100\text{ km/s}$ and $M = 1.8M_\odot$	30
4.14	The radial velocity profile for different ejection velocity parameters, v_i and α . As α increases, the velocity profile becomes linear.	32
4.15	The radial density profile for different ejection velocity parameters, v_i and α . The density is much steeper than a constant velocity model.	32

4.16	The radial temperature profile for different ejection velocity parameters, v_i and α . The temperature approaches $T \propto r^{-4/3}$, when v_i increases, which is the case of a constant velocity and no heating.	33
4.17	The absolute value of the heating and cooling mechanisms in the decreasing model, with $t = 1388$ years and $v(r = 0, t) = 165 * t^{-0.5}$ km/s. The dominant heating factor is the photoelectric heating, just weaker than the adiabatic cooling.	33
4.18	The spectra of $v(r = 0, t) = 165(t/\text{year})^{-\alpha}$ km/s, where α is varied between 0.1 and 1. The spectra are taken when the front of the gas reaches the outer edge of the outer shell.	34
4.19	The spectra of $v(r = 0) = v_i(t/\text{year})^{-0.8}$, where v_i is varied. The spectra are taken when the front of the gas reaches the outer edge of the outer shell.	35
4.20	The spectra of $v(r = 0) = 200(t/\text{year})^{-0.8}$ km/s, where the shell mass is varied. The spectra are taken when the front of the gas reaches the outer edge of the outer shell.	35
4.21	The best fit for the decreasing wind scenario to the SEST+ALMA data. The ejection velocity is $v(r = 0) = 200(t/\text{year})^{-0.8}$ km/s and a shell mass $2.97M_{\odot}$	36
4.22	The fit of an explosion model where the outer shell has a radius $75''$. The velocity parameters are $v_c = 160$ km/s and $v_o = 60$ km/s. The total gas mass in the ejection is $2.9M_{\odot}$	37
5.1	The spectra from the two scenarios' best models. The explosion model was ejected instantly with a Gaussian velocity distribution with the central velocity, $v_c = 100$ km/s and the velocity offset, $v_o = 60$ km/s. The total mass in the explosion was $1.4M_{\odot}$. The time decrease model used an ejection velocity $v(r = 0, t) = 200(t/\text{year})^{(-0.8)}$ and a shell mass $2.97M_{\odot}$	40
5.2	The velocity, density and temperature profiles from the two scenarios' best models. The explosion model was ejected instantly with a Gaussian velocity distribution with the central velocity, $v_c = 100$ km/s and the velocity offset, $v_o = 60$ km/s. The total mass in the explosion was $1.4M_{\odot}$. The time decrease model used an ejection velocity $v(r = 0, t) = 200(t/\text{year})^{(-0.8)}$ and a shell mass $2.97M_{\odot}$	40

1

Introduction

Stars are massive interstellar nuclear reactors in which new elements are created [1]. Without the stars there would not be any heavy elements. " We are all made of stardust " is an often repeated quote. Without the processes that occur in the stars, the giant element factories in the sky, there would be no Earth and there would not be any humans. The stars have an important role in the Universe and for life. That makes it very important to study them.

More than 400 years have passed since Giordano Bruno realized that the stars and the Sun were the same type of entity [1]. He was the first to propose that stars, just like the Sun, have their own planets and other objects orbiting them. There was an easy way to learn more about stars right in our back alley, by investigating our own star, the Sun.

In the last 400 years our understanding has increased vastly and recently more advanced telescopes and computers have made it easier for astronomers to study the stars. Nonetheless, there are still gaps to be filled by avid researchers. A lot is known about Sun-like stars, but exotic objects are often poorly understood. With more accurate telescopes distinct behaviors can be revealed, hidden in previous observations.

Stars, just like living beings, evolve through several phases [1]. A star spends most of its lifetime on what is called the main sequence, in hydrostatic equilibrium. Hydrostatic equilibrium implies that the nuclear fusion inside the star counterbalances the gravitational forces, preventing the star from imploding. When the nuclear fuel has been depleted within the core, the stellar structure readjusts to maintain the equilibrium. Stars with masses close to our Sun grows into giant stars with high mass loss rates [2]. After the star has ejected most of its material, the remnants of the central star can ionize it. With old telescopes, the ionized envelope looked similar to giant gas planets and is earning them the name "planetary nebula".

The target of this thesis is the Boomerang Nebula which is a preplanetary nebula. In Preplanetary nebulae the outflow has not yet been ionized [3]. Compared to other preplanetary nebulae, the Boomerang Nebula holds several distinguishing features that separate it from its kin. Its rarest feature is its outflow which is the coldest known naturally occurring medium in the Universe [4].

The Boomerang Nebula was first observed in detail by Sahai and Nyman 1995 [4]. To fit the observations, they constructed a model with an assumption that the outflow had a constant velocity in the cold region. However new measurements from 2013 showed a multitude of velocities [5]. The velocity of the outflow had to have a radial dependence. The main goal of this thesis is to obtain a deeper understanding of the radial dependence of the outflow velocity. By understanding the behavior of unique

objects such as the Boomerang Nebula, we will improve our understanding of the late phases of stellar evolution.

The first chapter is an introduction chapter, which gives a quantitative description and introduces the reader to the subject. It covers the units that are used in astronomy, as well as a short tour of stellar evolution. The third chapter's focus is stellar wind models and how they can be used to describe the Boomerang Nebula's outflow. The fourth chapter contains the motivation to this thesis and a description of the methods. The fifth chapter shows the result of the modelling and comparisons with observations. In the sixth chapter the results are discussed. The seventh and final chapter gives an outlook on future uses of the work in this thesis. It also covers potential upgrades to the models and the next steps necessary to understand the Boomerang Nebula.

1.1 Units

It is no longer convenient to use standard SI units when working with the large scales in astronomy. While a meter or a kilogram works great when dealing with every day life, larger units are required when working with the large scales of the Universe.

For example, astronomers count mass in solar masses, M_{\odot} [1]. A solar mass is

$$M_{\odot} = 1.989 \times 10^{30} \text{ kg.} \quad (1.1)$$

The lifetime of a star is in scales of millions or billions of years, so during a second only an insignificant amount of mass is lost. The commonly used unit used for mass-loss rate of stars is M_{\odot}/year [1], where

$$1M_{\odot}/\text{year} = 6.305 \times 10^{22} \text{ kg/s.} \quad (1.2)$$

The movement of stellar objects tends to be estimated in kilometers per second. Giant stars can eject material moving at 500 km/s. Comparatively the speed of a bullet is 1 km/s. And while a bullet hits a wall within a few seconds, the ejected material moves freely. During a year, a short time compared to the stellar lifetimes, the ejected material travels 2×10^{10} km. During the same time starlight travels 9×10^{12} km. These distances, which normally would seem immense, are quite small in the Universe. Measuring the large distances light and matter travel in space requires much larger units than measuring distances on Earth.

Different units are chosen based on context. For describing the close environment of a stellar object, the common choice is astronomical units (AU), where

$$1 \text{ AU} = 1.496 \times 10^{11} \text{ m.} \quad (1.3)$$

1 AU is the distance between the Earth and the Sun, or more explicitly since the Earth's orbit around the Sun is elliptical, it is defined as the average of the minimum and maximum distance between them [1]. Initially this distance was calculated using the parallax method, which is still used to calculate the distance to stars.

The parallax method uses the angle between a near object and a distant object [1]. When the observer moves, the nearer object seems to move with respect to the

farther away one. With the distant object as a reference point, the change in the angle between the two points can be noted. The parallax angle, p , is defined as half this change in angle, and with triangulation the distance to the nearby object is

$$D = \frac{d}{\tan(p)}, \quad (1.4)$$

where d is half the distance between the observation points.

The distance to other stars is so large that the parallax between two locations on earth is too small to be measured accurately. Instead the parallax angle is observed with a six month interval. In this time the Earth has travelled halfway around the Sun so that $d = 1$ AU. This distance is many magnitude larger than the Earth radius giving much more accurate results.

But even when using the orbit of the earth, the parallax angle is still very small. Instead of degrees, astronomers use arc minutes and arc seconds for the parallax angle.

An arc minute, or $1'$, is defined as one sixtieth of a degree and similarly an arc second, or $1''$, is one sixtieth arc minute. The unit for the distance to stars is

$$1 \text{ parsec} = \frac{1 \text{ AU}}{\tan(1'')} = 3.086 \times 10^{16} \text{ m}, \quad (1.5)$$

These units are necessary to know for reading astronomy papers, but more important to understand are the processes in the Galaxy. Next follows an introduction of the creation of the stars and their impact on the Galaxy.

1.2 Star formation and the main sequence

Our galaxy is not only stars and empty space. The medium between the stars, called the interstellar medium (ISM), contains gas and dust [6]. 91% of the gas atoms in the ISM are hydrogen. The second most prevalent element in the ISM is helium, accounting for most of the remaining 9%. The relationship between stars and the gas is cyclical, the stars are born from the gas and during their lifetime the stars push it back into space.

More specifically, stars are born within giant molecular clouds (GMCs). GMCs are humongous clouds of molecular gas, with diameters up too 100 parsec [7]. Just like stars, the GMCs are in hydrostatic equilibrium [6]. But eventually instabilities within the cloud lead to the collapse of pockets of gas. The molecular gas from the GMC is condensed in a few dense cores. At the center of each core a protostar forms.

The accreted material have small rotational velocities which, to preserve the angular momentum, cause the cores to spin faster and faster. Like a pizza, the cores flatten and form a preplanetary disc around the protostar. The protostar starts ejecting matter perpendicular to its rotation. As the preplanetary disc spins, the dust in the disc combines into larger and larger grains of dust. After millions of years, most of the dust has bundled together into planets and other objects such as asteroids.

In the protostar, the compression due to gravity leads to an increase in density, temperature and pressure. When the pressure is high enough to counterbalance

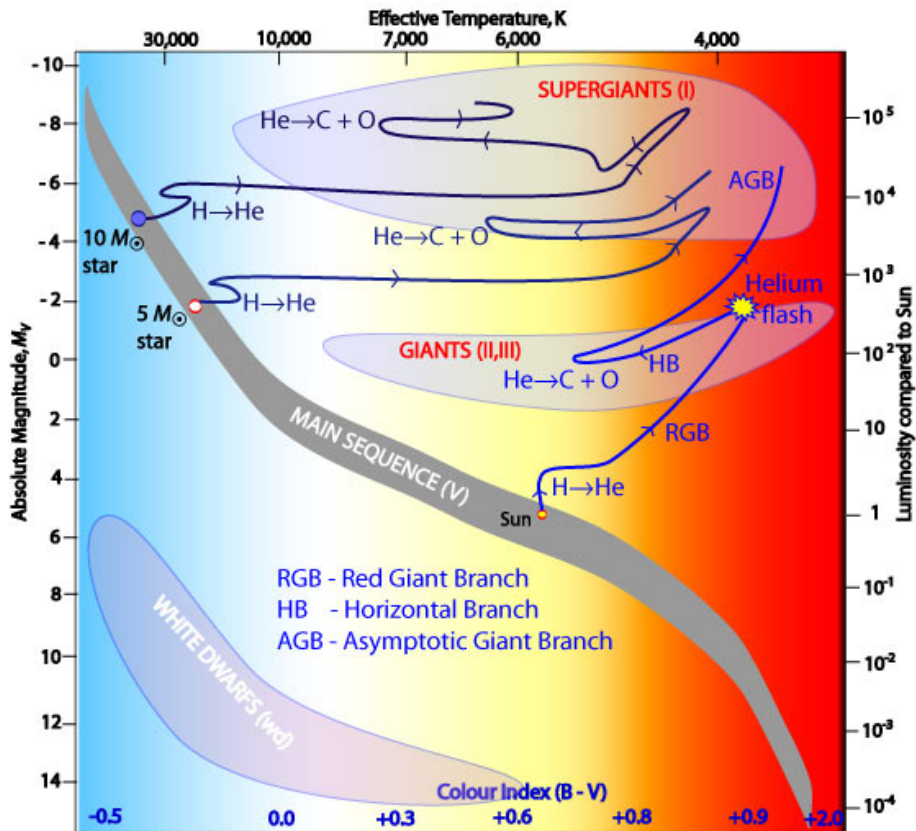


Figure 1.1: A Hertzsprung Russel diagram showing the relationship between the luminosity and the temperature of a star. This plot clearly shows the main sequence full of young stars. The central star of the Boomerang Nebula is a post-AGB star. It has just left the AGB branch and is on it's way to become a white dwarf. [1]

the gravity the cloud regains hydrostatic equilibrium. The collapse stops, but the protostar is too cold for nuclear fusion.

At a temperature of around 2000 K, the thermal energy causes the molecular hydrogen inside the nucleus of the core to dissociate [8]. Soon after, the hydrogen and the helium are ionized, and at 10^7 K, the Star's nucleosynthesis can start [9]. At the protostar's nucleus the hydrogen atoms fuse into helium, releasing energy. Since this process is exothermic, it is called hydrogen burning.

When the hydrogen burning starts the protostar has transformed into a star. The newborn star is located on the main sequence, where it will spend 90 % of its lifetime [1]. Stars in the main sequence are in hydrostatic and thermal equilibrium. Thermal equilibrium states that the energy generation of the star is balanced by it's luminosity. The correlation between stars in the main sequence can be seen in a Hertzsprung-Russel (HR) diagram (see Figure 1.1). The HR diagram shows the relationship between the luminosity and the effective temperature of the stars. Depending on a star's position on the HR diagram its evolutionary phase can be inferred.

When the nucleus of a main sequence star is depleted of hydrogen, it is impossible for hydrogen burning to continue within it [3]. With no hydrogen burning, there is no pressure to balance out the gravity. This causes the nucleus to lose hydrostatic equilibrium and collapse. The gravitational energy is converted into thermal energy, increasing the temperature and triggering hydrogen burning in a shell around the core. The helium produced in the shell falls back into the core, increasing the core's density and temperature.

1.3 Red giant branch and asymptotic giant branch

The higher temperature enables higher rates of hydrogen burning in the shell than earlier within the nucleus. The increase in energy output causes the star to expand to several magnitudes bigger than its main sequence size. As the surface area of the star increases the surface temperature decreases. The nucleus is hot and massive, while the star has a low effective temperature and a critically low density. Due to the color and the size of the star, it is labeled as a red giant. Red giants are located on the red giant branch (RGB) in the HR diagram (Figure 1.1).

When the nucleus has reached a temperature of 10^8K the helium fuses into beryllium [3]. Through fusing with other helium atoms, it forms carbon and then oxygen. During this process, called helium burning, the star's effective temperature is increasing with conserved luminosity. The star simultaneously burns helium in its nucleus and hydrogen in a shell. After this phase, called the horizontal branch (HB), the star enters the asymptotic giant branch (AGB).

During the HB, the nucleus expends its helium [3]. Left in the nucleus is carbon and oxygen, with too low temperature for them to fuse. Instead helium burning starts in a shell around the nucleus. The star is again a red giant. The AGB is said to be asymptotic since it approaches the RGB asymptotically in the HR diagram.

After the helium shell is depleted, the star derives its energy from hydrogen burning in a thin hydrogen shell [2]. The helium produced forms a thin layer of helium between the hydrogen shell and the nucleus. When enough helium has been accumulated, helium burning is reignited. The helium burning will push out the hydrogen shell and extinguish the burning there. This process is referred to as a thermal pulse. After the thermal pulse, hydrogen burning is reignited in the the shell accumulating more helium for another thermal pulse (see Figure 1.2). Thermal pulses increase the luminosity and size of the star periodically. During the pulses, and to a lesser extent during the entire AGB phase, a lot of mass is ejected into the star's circumstellar environment.

1.4 Planetary nebulae

When an AGB star has ejected almost all of its hydrogen envelope, it will enter the preplanetary nebula (PPN) phase [2]. When looking at PPNs, the focus does not lie on the central star, but instead on the ejected material. This is because the ejected gas can be many times the mass of the star.

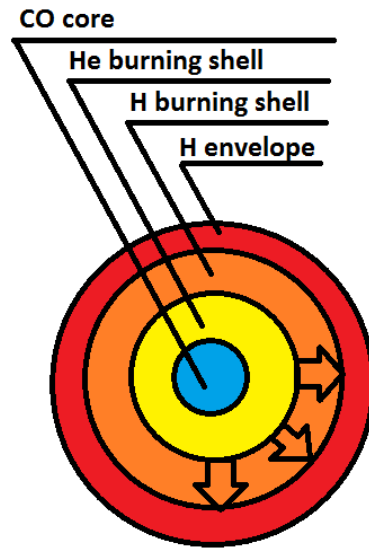


Figure 1.2: A schematic view of the AGB star during thermal pulses. Hydrogen burning happens in the envelope of the star producing helium. When enough helium has been created, helium burning is reignited pushing out the hydrogen envelope.

During the PPN phase, the central star is too cold to ionize the ejected material. Preplanetary nebulae are said to be reflection nebulae. Reflection nebulae have very little emission in the visible spectra and were originally detected by the scattering of the light from their central stars.

From the hydrogen burning in the shell, the star's effective temperature is increasing. When the central star has become hot enough to produce ultraviolet light, it ionizes the ejected envelope. The ionized envelope becomes an emission nebula, showing an appearance similar to giant gas planets such as Jupiter.

The star has entered the planetary nebula (PN) phase. The PN phase is the star's last high-luminosity phase. When the hydrogen shell exhausts, the central star becomes too cold to ionize its increasingly distant gas cloud and become a white dwarf. White dwarfs are dense stars, with no internal source of energy. Meanwhile the gas cloud turns invisible, ending the planetary nebula phase.

Planetary nebulae comes in various shapes [10]. Everything from bipolar and disc-shaped to quadripolar and point-symmetric planetary nebulae have been observed. The morphology of the planetary nebulae is highly dependent by how it acts during the PPN phase. One of the reasons to study the Boomerang Nebula is to understand how the shaping of PN takes place.

1.5 Stellar effects on the ISM

While most stars enter the RGB after depleting hydrogen in their nuclei, not all of them do. Main sequence stars with a mass below $0.5 M_{\odot}$ never become hot enough to initiate helium burning. Instead they cool down and turn into white dwarfs [1]. Stars with high mass also have unique features, main sequence stars heavier than

$2 M_{\odot}$ smoothly proceeds with helium burning after the hydrogen is depleted. They then have helium burning and hydrogen burning in their shell simultaneously. Stars with a main sequence mass above $8 M_{\odot}$ are able to burn the carbon within its core to produce magnesium [2]. Heavier elements are produced in supergiants, stars with main sequence masses above $10 M_{\odot}$, named as they grow much larger than other stars [11]. Super giants are composed of several shells, each with different elements burning, and eventually build up an iron nucleus [12].

When a super giant depletes its fuel, it collapses into a supernova. Supernovae are titanic explosions able to outshine entire galaxies [1]. The total radiant energy of a supernovae is the same as our Sun will produce during its entire life. The high energy of supernovae make them the most energetic nuclear reactors in the Universe. Most natural elements heavier than iron are produced in supernovae. The exception is specific elements created through slow neutron capture processes in AGB stars' shell.

From the chemical composition of the ISM it is possible to learn about nearby stars. While most helium and hydrogen were created in the Big Bang, heavier elements are often created in stars [1]. And generally, the heavier an element is, the bigger was the nuclear reactor it was produced in.

It is not only gas that the stars eject into ISM, but also dust. Most of the cosmic dust in the ISM is formed in AGB stars or supernovae [2]. Just like the gas can be traced to its progenitors, so can the dust. Stars with more oxygen than carbon produce oxygen rich dust, oxides and silicates, and stars with more carbon produce carbon rich dust, carbocaneous dust. Supernovae have both carbon rich and oxygen rich layers and therefore can produce both kind of dust. But since most of the layers are oxygen rich, the dust from supernovae are dominantly silicates. All AGB stars are initially oxygen rich, But AGB stars with a mass between $\approx 1.6 M_{\odot}$ to $4 M_{\odot}$ will become carbon rich. Therefore, the surrounding dust contain information about the chemical structure of the stars, as well as limits to an AGB star's mass.

1.6 Boomerang Nebula

The Boomerang Nebula is a biconal preplanetary nebula, discovered by Wegner and Glass in 1979 [13]. Its most unique feature is its outflow, which is the coldest known natural occurring object in the entire Universe [4]. As a remnant of the Big Bang, the Universe is coated with Cosmic Microwave Background Radiation (CMBR), with a characteristic temperature around 2.7 K. Normally the CMBR has to be treated as noise, as the emission from stars towers about it, but the Boomerang Nebula's outflow is cold enough to absorb the photons emitted from the CMBR. By absorbing the CMBR photons, the outflow is self-shielded and the CMBR photons can not penetrate and heat the innermost regions.

Another interesting aspect of the Boomerang Nebula, and bipolar nebulae in general, is that the outflow seems to carry a much larger amount of linear momentum than expected from the current model for radiation-pressure-driven outflows in evolved stars. The mechanism behind the driving of these winds is not understood and is one of the reasons for studying these enigmatic objects [14].

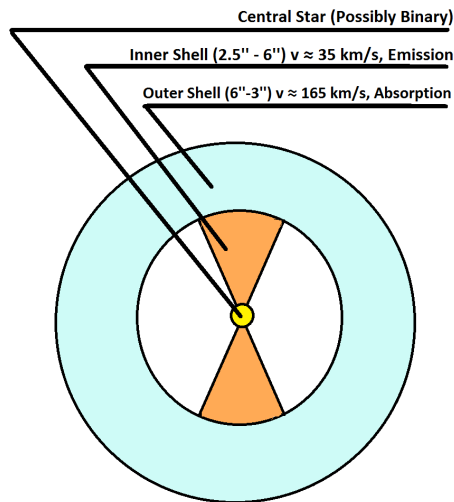


Figure 1.3: A schematic view of the Boomerang Nebula and its shell. The focus of this thesis is the Nebula’s absorbing outer shell, the coldest known naturally occurring object in the Universe.

The outflow of the Boomerang Nebula is separated in two distinct shells [4], illustrated in Figure 1.3. The inner shell is biconical, with a temperature slightly above the CMBR and a velocity around 35 km/s. It is located between 2.5'' (3743 AU) and 6'' (8690 AU) from the central star. The outer shell, which is colder than the CMBR, is located between 6'' (8690 AU) and 33'' (48129 AU). It does not follow the biconal shape of the inside and is instead almost spherical. The outer shell has a multitudes of velocities, peaking at around 165 km/s.

In the outflow, the hydrogen has returned to its molecular state. Even if hydrogen is the most dominant element in the molecular gas, molecular hydrogen has no permanent dipole moment [6]. It radiates very poorly at radio wavelengths, making it difficult to detect. Due to this, other molecules are used to trace the outflow. A good tracer is carbon monoxide (CO). CO has stable bonds and several emissions in the radio spectrum.

1.7 Probing the circumstellar environment

When a molecule changes state, it absorbs or emits a photon [15]. These photons, detectable with telescopes, give us information about distant objects. The energy levels, or states, of the molecules are quantized so that when a molecule absorbs or emits a photon, its frequency and energy can be related to a state transition.

Molecules have three different kinds of state transitions [15]. The most energetic transitions are electronical. These transitions happen when the electrons inside the molecules are excited or deexcited, emitting UV photons. The second most energetic are the vibrational transitions. When the molecules transit between vibrational states they emit infrared (IR) photons. The least energetic transitions of the molecules are the rotational transitions. The rotational transitions emit photons in the radio, sub-millimeter and IR wavelengths. Radio photons can be detected on

the Earth's surface, while UV and IR photons are blocked by the atmosphere. Due to this, the rotational transitions are often the ones that can be observed in the greatest detail.

Rotational transitions can be modelled as a rigid rotor [1]. In classical physics the energy of a rigid rotor is $E_{rot} = \frac{L^2}{2I}$, where L is the angular momentum and I is the rotor's moment of inertia. Similarly the energy of the rotation states are

$$E(J) = \frac{J(J+1)h^2}{8\pi^2I} = B_0J(J+1). \quad (1.6)$$

In this equation, J is the quantum number for the rotational states, with $J = 0$ being the rotational ground state. Linear molecules, like CO, follows the rotational transition rule, $\Delta J \pm 1$. The constant, h , in the equation is Planck's constant. The energy of a photon that is emitted from $J \rightarrow J - 1$ is

$$E_{photon} = \Delta E(J) = E(J) - E(J-1) = B_0(J(J+1) - J(J-1)) = 2B_0J. \quad (1.7)$$

For example, CO has the rotational constant $B_0 = 0.238$ meV [6]. Equation (1.7) then states that the rotational transition CO($J = 1 \rightarrow 0$) emits a photon with an energy of 0.476 meV. From Planck's relation the frequency of the photon is 115.27 GHz. Planck's relation correlates the energy, E_{photon} with the frequency, ν as

$$E_{photon} = h\nu. \quad (1.8)$$

The emission lines can be used to obtain the target's minimum temperature [6]. The thermal energy of an object is given as $E_t = k_B T$, where k_B is the Boltzmann constant and T is the target's temperature. For example, for CO to continually emit CO($J = 2 \rightarrow 1$), the molecules need to be excited to the second rotational level. Using Equation (1.6) and $B_0 = 0.238$ meV, $T \geq \frac{6B_0}{k_b} = 16.6$ K.

Normally the emission source is moving, so that the frequency will be shifted by the Doppler effect [1]. The Doppler effect is a relativistic effect. It states that if the emission source is moving at a velocity, Δv , relative to the observer, the observer sees a photon with frequency

$$\nu_c = \nu_0 \left(1 + \frac{\Delta v}{c}\right). \quad (1.9)$$

Here, c , is the speed of light and, ν_0 , is the emission frequency excluding the Doppler effect. While it may require more than one emission peak to find Δv , the relative velocity is useful information of the target.

The Doppler effect also has another impact on the emission line. Since the Doppler shift perceived by an observer is determined by the velocity component along the line of sight, different regions of a circumstellar envelope expanding with velocity v will present different Doppler shifts. A given observed line is said to be broadened by this effect. The projected velocity changes gradually from $-v$ for gas in the part of the envelope moving away from the observer to 0 in the plane of the sky to v in the part of the envelope approaching the observer. On top of this, any radial variations of the expansion velocity may also contribute to the broadening of a given line.

1.8 Telescopes

Measuring the emission lines of stellar objects, thousands of parsecs away, requires large telescopes with advanced equipments. The angular resolution of a telescope is inversely proportional to its aperture diameter [16].

This thesis uses data sets obtained with two different telescopes. The first was obtained in 1997 by Sahai and Nyman with the Swedish-ESO Submillimeter Telescope (SEST) [4]. SEST was a radio telescope in La Silla, Chile, that was active between 1987 and 2003 [17]. It had an aperture diameter of 15 m and, for the CO($J = 1 - 0$), an angular resolution of $42''$. As the Angular resolution was larger than the Boomerang Nebula (see Figure 1.3), the observation did not provide much details on the velocity dispersion.

The second data set was obtained in 2013 by Sahai et al. with the Atacama Large Millimeter/submillimeter Array (ALMA) [5], also located in Chile. ALMA used an array of 33 telescopes to virtually increase the aperture. In total, ALMA has 55 telescopes [18], moveable to span an aperture with a diameter of 16 km. With ALMA, it was possible to reduce the angular resolution down to less than $5''$, smaller than the outer shell.

2

Stellar Winds

Outflows that originate from stellar atmospheres are called stellar winds [6]. The focus of this thesis is to model the velocity dependence of the outflow in the outer shell of the Boomerang Nebula.

Stellar winds collide with gas in the ISM or the circumstellar envelope. These can usually be distinguished based on differences in parameters such as velocity, density and temperature. The goal of the wind model is to obtain such parameters for the Boomerang Nebula's outflow. They can be obtained from radiative transfer model, since the emission from the outflow depends on its parameters.

Stellar wind models assume that mass, momentum and energy are conserved [19]. The mass conservation can be modeled by the mass continuity equation

$$\frac{\partial \rho(\vec{r})}{\partial t} + \nabla \cdot \rho(\vec{r})\vec{v}(\vec{r}) = 0. \quad (2.1)$$

The mass continuity equation has a spatial dependence, using \vec{r} as the position vector. At \vec{r} the density is $\rho(\vec{r})$ and the outflow velocity is $\vec{v}(\vec{r})$.

The mass continuity equation can be related to the star's mass loss \dot{M} with two assumptions. The first assumption is spherical symmetry, that the outflow is symmetric in all directions from the star. The distance to the center of the star r can replace \vec{r} .

The second assumption is that the system is in steady state. This means that the stellar wind properties are constant in time. Under these assumptions Equation (2.1) can be rewritten as

$$\dot{M} = 4\pi\rho v r^2. \quad (2.2)$$

Equation (2.2) is irrelevant for an outflow with a radial dependence, but is useful for showing relations between parameters in stellar wind models.

The second quantity that is conserved is momentum, for which the conservation equation is

$$\frac{\partial \vec{v}(\vec{r})}{\partial t} + \vec{v}(\vec{r}) \cdot \nabla \vec{v}(\vec{r}) = -\frac{\nabla P(\vec{r})}{\rho(\vec{r})} - \frac{GM}{r^2}\hat{r}. \quad (2.3)$$

P is the radiation pressure, G is Newton's gravitational constant and M is the mass of the star. In the outer shell of the Boomerang Nebula we have a large distance and a high velocity. Due to this, the contributions from the pressure and gravity are negligible. Under these assumptions Equation (2.3) can be reduced to

$$\frac{\partial \vec{v}(\vec{r})}{\partial t} + \vec{v}(\vec{r}) \cdot \nabla \vec{v}(\vec{r}) = 0. \quad (2.4)$$

This equation can be fulfilled with simple Newtonian mechanics. It is assumed that the wind can move freely in space without outer constraints. It is simple to obtain the radial dependencies of the density and velocity. But to obtain the radial profiles of the temperature, it is required to consider the heating and cooling processes in the outflow.

2.1 Heating and cooling processes

The radial dependence of the temperature can be modeled as [20]

$$\frac{dT(r)}{dr} = (2 - 2\gamma)\left(1 + \frac{r}{2v(r)} \frac{\partial v(r)}{\partial r}\right) \frac{T(r)}{r} + \frac{\gamma - 1}{n_{H_2}(r)k_B v(r)}(H - C). \quad (2.5)$$

The first term covers the adiabatic cooling. The adiabatic cooling is the dominant cooling process in the outflow, caused by pressure decrease in a system [21]. The common gas law states that a decrease in pressure makes it expand. But a system with neither matter or heat output is adiabatically isolated. When an adiabatically isolated system expands, it does work on its surrounding, cooling itself. In the adiabatic cooling term, T is the outflow temperature and γ is the heat capacity ratio. The heat capacity ratio can be related to the degrees of freedom of the gas, f ,

$$\gamma = \frac{f}{f + 2}. \quad (2.6)$$

At $T \leq 300$, the rotational excitations of H_2 , the dominant molecules in the molecular gas, are insignificant. Due to this the molecular gas can be treated as a monoatomic gas with $f = 3$ and $\gamma = 5/3$.

The second term in Equation (2.5) contains the molecular heating and cooling processes in the outflow. Here n_{H_2} is the number density of the molecular gas, which is related to the mass density by $\rho_{H_2} = m_{H_2}n_{H_2}$, where m_{H_2} is the mass of a H_2 molecule. The constant k_B is the Boltzmann constant, relating the system's thermal energy and temperature, $E_t = k_B T$. Finally $H - C$ is the sum of the heating and cooling rates.

The dominant heating processes are dust-gas collisional heating, dust-gas adhesion heating and photoelectric heating [22].

The dust-gas collisional heating [20] comes from gas colliding with dust and is modelled with

$$H_{dg} = \frac{3}{8}m_{H_2}(n_{H_2}(r))^2 \frac{\Psi}{a_g \rho_g} \frac{v_{drift}^3}{1 + \frac{v_{drift}}{v(r)}}. \quad (2.7)$$

The dust properties is the dust-to-gas mass ratio, Ψ , the average dust grain radius, a_g and the average dust grain density, ρ_g . The model assumed silicate dust with $\Psi = 0.01$, $a_g = 0.1 \mu\text{m}$ and $\rho_g = 3.3 \text{ g/cm}^3$. Another dust property is the drift velocity of the dust through the gas, v_{drift} . This is assumed to be constant at $v_{drift} = 10 \text{ km/s}$.

The dust adhesion heating [23] can be modelled as

$$H_{dt} = 2.008 \times 10^{-31} (n_{H_2}(r))^2 \frac{\Psi}{a_g \rho_g} \sqrt{T(r)(T_{dust} - T(r))} (0.35e^{-\sqrt{\frac{T_{dust} + T(r)}{500}}} + 0.1). \quad (2.8)$$

The expression contains the dust temperature T_{dust} , which has been assumed to be constant at $15K$. Note that the equation assumes SI units.

The final heating contribution that was considered is the photo-electric heating, which is the heating of the gas from stray photons. It is covered in

$$H_{pe} = K_{pe}n_{H_2}(r), \quad (2.9)$$

where $K_{pe} = 10^{-33}$ J/s [24].

The only non-adiabatic cooling term able to affect the temperature is the H_2 vibrational line cooling [23],

$$C_{H_2} = 2.611 \times 10^{-34}n_{H_2}(r)\left(\frac{T_{kin}}{1000}\right)^{4.74}. \quad (2.10)$$

From putting all the heating and cooling factors together in Equation (2.5), the temperature's radial dependence can be obtained.

The photoelectric heating came from photons stimulating electronial transitions in the gas, but if the photons are energetic enough they are able to dissociate the molecular gas into atoms.

2.2 Photodissociation

At the inner regions of the circumstellar envelope the molecules are shielded by the gas in the outer region. But in outer regions, the molecular bonds break from interactions with high energy photons from the ISM. At the so called dissociation radius, half of the molecules in the gas have dissociated. The dissociation radius varies between different molecules, relative to their dissociation energy, which is the minimum energy for a photon to dissociate it [25].

The high dissociation energy of CO is one of the properties that makes it a good tracer molecule. But even if the dissociation radius of CO is large, it is not infinite. Outside of its dissociation radius the CO dissociates into C and O atoms. And although the stellar wind continues, the CO emission or absorption lines disappear.

3

Motivation and methods

The Boomerang Nebula was initially discovered in 1978 by Wegner and Glass [13]. In 1997 its molecular outflow was observed by Sahai and Nyman with SEST (Swedish ESO Submillimeter Telescope) [4]. They discovered that the nebula's outflow is colder than the cosmic microwave background radiation (CMBR). The CMBR is a remnant from the Big Bang maintaining the Universe's temperature at 2.7 K. The outer shell of the Boomerang Nebula (see Figure 1.3) by mimicking the behavior of a refrigerator. It cools through adiabatic cooling and self-shields from the CMBR. But the Boomerang Nebula is not only colder than the CMBR, it is also the coldest known naturally occurring object.

The SEST spectrum of the $\text{CO}(J = 1 - 0)$ transition shows absorption in velocities ranging from roughly -165 km/s to 165 km/s. As explained at the end of Section 1.7, this is caused by Doppler line broadening and reflects the velocity dispersion in the shell. The SEST spectrum had a beam size of $40''$, and resembled the first plot in Figure 3.1. It shows a wide velocity dispersion that could be explained using many different models. The emission at the center of the spectrum originates in the inner shell (see Figure 1.3) and is not considered in the thesis.

Further observations of the Boomerang Nebula were done by Sahai et al. in 2013 with ALMA [5], which used an array of several telescopes to simulate a smaller beam size. The beam, which was not circular, had a major axis of $4.12''$ and its minor axis of $1.83''$. Figure 3.1 depicts ALMA observations which show that even for smaller beam sizes, the outer shell shows absorption in a wide range of velocities.

Sahai and Nyman constructed a model with a constant expansion velocity, that could fit well to the SEST spectrum (see figure 3.2) [4]. However, a constant velocity model produces two sharp absorption peaks when imaged with a small aperture (see the last plot in Figure 3.2), in contrast to what is seen in the ALMA observations.

To address this problem, two different scenarios with radially dependent outflow velocities were considered. The first one is an initial explosion ejecting most of the gas into the envelope. The second scenario is an outflow with a time-varying ejection velocity. The scenarios were modelled independently and their parameters were adjusted to match the ALMA and SEST data.

The outflow was simulated in MATLAB. Assuming spherical symmetry the outflow could be modelled with one dimensional mass bins. And assuming that the radiation pressure and gravitation had negligible effect, the gas could move freely. The outflow simulations output the radial profiles of velocity, density and temperature. The profiles were input into a radiative transfer (RT) model to simulate how light propagated inside the outflow. The RT model produced the $\text{CO}(J = 1 - 0)$ line that

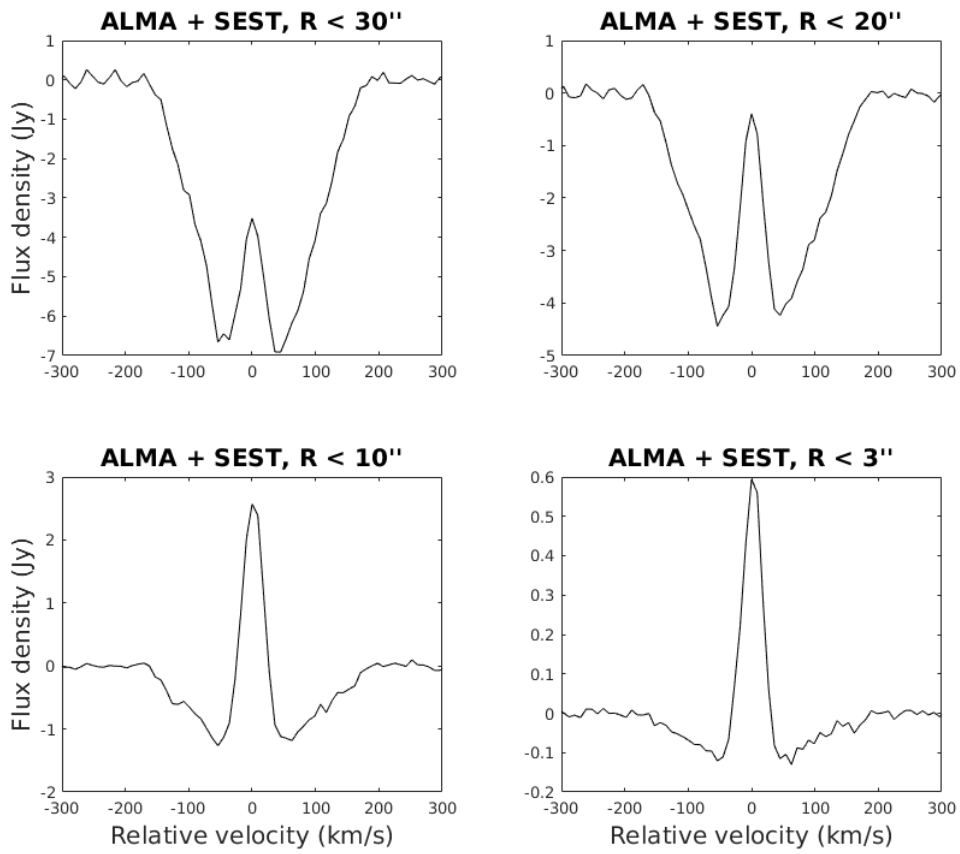


Figure 3.1: The spectra of the CO($J = 1 - 0$) line from the SEST+ALMA data, given at four different apertures. The spectrum in the upper-left panel is similar to the SEST spectrum, while the spectrum in the lower-right panel was obtained from a much smaller aperture.

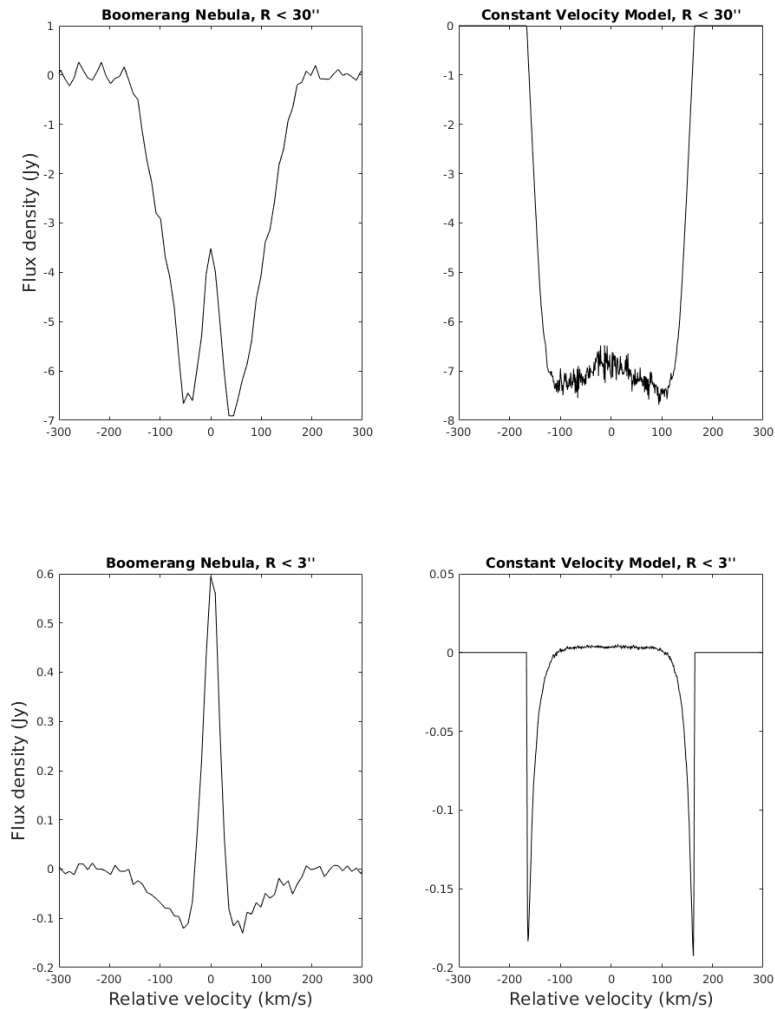


Figure 3.2: The first upper-left panel shows the $\text{CO}(J = 1 - 0)$ line from a large aperture around the Boomerang Nebula. It is included to show how the original SEST data looked like. From the spectrum, it is hard to say anything about the velocity’s radial behavior. In the center of the line, there is emission from the inner shell. The upper-right panel shows the same line for a constant velocity model, to show that it is possible to describe the SEST data with it. The lower-left panel shows the CO line extracted from the ALMA data using an aperture smaller than the shell. The lower-right panel shows how a constant velocity model would look in the same aperture. A constant velocity model is not able to describe the ALMA spectrum and, hence, a model with a radially dependent velocity profile is required.

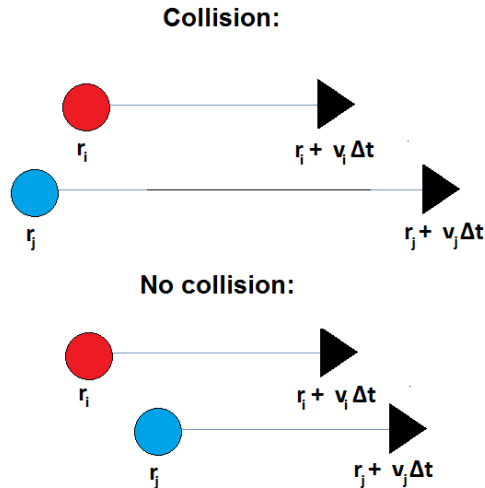


Figure 3.3: How the simulation determined if two mass bins collided. The particles had positions r_i and r_j and velocities v_i and v_j respectively.

were compared with the observations.

3.1 Outflow simulations

The mass bins were ejected from the central star with an initial velocity that depended on the scenario. After a time step Δt , a given mass bin located at r_i with velocity v_i moved to a new position.

$$r'_i = r_i + v_i \Delta t. \quad (3.1)$$

The simulations included collisions when one mass bin encountered others. Given a second mass bin located at r_j with velocity v_j , it will collide with the first mass bin if $r_j \leq r_i$ and $r_j + v_j \Delta t \geq r_i + v_i \Delta t$ (see Figure 3.3). If these criteria were obeyed for several mass bins, it was treated as a multibody collision. In the simulations all mass bins had the same mass m and the collisions were considered elastic. Therefore after a collision, the mass bins had a velocity equal to their mean velocity.

The velocity profile, $v(r)$, was the mean velocity of all mass bins between r and $r + \delta r$, where δr is the radial resolution. Similarly the density profile was

$$\rho(r) = m \frac{3dN}{4\pi((r + \delta r)^3 - r^3)}, \quad (3.2)$$

where dN is the amount of mass bins between r and $r + \delta r$ and m is the mass of a mass bin.

3.1.1 Explosion scenario

In the explosion scenario, all the mass bins were ejected at $t = 0$, with a Gaussian velocity distribution

$$f(v) = \frac{1}{v_o\sqrt{2\pi}} e^{-\frac{(v-v_c)^2}{2v_o^2}}. \quad (3.3)$$

Here v_c is the central velocity and v_o is the standard deviation of the distribution. The standard deviation is the square root of the expected value of $(v - v_c)^2$. These two parameters could be adjusted for matching the ALMA data. The third parameter was the total ejected mass M , which was related to the density as $M = mn_{bins}$. Here n_{bins} is the total amount of mass bins in the model, and serves as a resolution parameter for the model.

3.1.2 Decreasing velocity scenario

The second scenario used

$$v(r=0) = v_i \left(\frac{t}{t_0}\right)^{-\alpha}, \quad (3.4)$$

where α and v_i are adjustable parameters. The outflow starts ejecting at the time t_0 with the initial ejection velocity v_i . If $\alpha < 0$ a snowplow effect would be created, gathering the gas in a single wavefront. This is inconsistent with the ALMA data, so α must be positive. It was also assumed that the mass loss rate \dot{M} was constant. The mass bin mass could be related to the mass loss rate as

$$m = \dot{M}dt, \quad (3.5)$$

where dt is the time difference between the ejection of two mass bins. Just like n_{bins} , dt is another resolution parameter. The parameter used for scaling the density was M_{shell} , which is the mass that has entered the shell.

$$M_{shell} = \dot{M}(dt_{shell}), \quad (3.6)$$

where dt_{shell} is the time between the ejection of the first and the last mass bins in the shell.

3.1.3 Temperature profile

The temperature profile was calculated in the same way for both models, and required the density and velocity profiles as input. At the inner edge of the cold region (see Figure 1.3), the temperature was set to the CMBR temperature, $T(8690 \text{ AU}) = 2.725 \text{ K}$. Thereafter the temperature was integrated stepwise with the different heating contributions in Equation (2.5),

$$T(r+dr) = T(r) + \frac{dT}{dr}(r)dr. \quad (3.7)$$

3.2 Radiative transfer

The velocity, density and temperature profiles were input into a radiative transfer (RT) software called LIME [26]. RT is the study of how photons propagate within

a medium. RT modelling can be done analytically for simple morphologies, but for more complex ones even numerical solutions require extensive calculations. LIME is a software created by C. Brinch and M. R. Hogerheijde for RT solutions at millimeter and far-infrared wavelengths [26].

LIME received as input the velocity, density and temperature profiles together with CO properties to create an image cube of the CO($J = 1 - 0$) line. Image cubes contain the intensity as a function of longitude, latitude and the velocity along the line of sight. Spectra were extracted from the image cube with the Common Astronomy Software Applications (CASA), an applications package constructed for data post-processing. The spectra were extracted from apertures with two different radii to examine the stellar wind parameters' impact on the line shape. The parameters were then adjusted in an attempt to fit the ALMA data.

LIME like other RT models is based on the equation of RT [1],

$$\frac{dI_\nu}{ds} = j_\nu - \alpha_\nu I_\nu. \quad (3.8)$$

The equation of RT depicts how the intensity, I_ν , in a given frequency, ν , changes along a path, s , through a medium. The parameters, j_ν and α_ν , are the emission coefficient and the absorption coefficient, based on the medium along the path [1]. The coefficients differ for dust and for gas, where the dust-to-gas ratio was assumed to be 0.01. For gas

$$\begin{aligned} j_\nu^{gas} &= \frac{h\nu}{4\pi} n_2 A_{12} \Phi(\nu) \\ \alpha_\nu^{gas} &= \frac{h\nu}{4\pi} (n_1 B_{12} - n_2 B_{21}) \Phi(\nu), \end{aligned} \quad (3.9)$$

where A_{12} , B_{12} and B_{21} are the Einstein coefficients [26], which define the emission and absorption probabilities for a transition between two states with densities, n_1 and n_2 . A_{12} is the probability of spontaneous emission, B_{12} of absorption and B_{21} of stimulated emission. The energy difference between the states is $E_2 - E_1 = \Delta E = h\nu$, with h as Planck's constant. The function $\Phi(\nu)$ is a line broadening function built on several mechanisms, with the dominant mechanism being the Doppler line broadening from the velocity dispersion.

The emission and absorption coefficients in dust are

$$\begin{aligned} j_\nu^{dust} &= -\alpha_\nu^{gas} B_\nu(T_{dust}) \\ \alpha_\nu^{dust} &= \kappa_\nu \rho_{dust}. \end{aligned} \quad (3.10)$$

For calculating the dust coefficients, the dust opacity, κ_ν , the dust temperature, T_{dust} , and the dust density, ρ_{dust} , are necessary. The dust opacity were input into the model, T_{dust} was assumed as equal to the gas temperature, T_{gas} , and ρ_{dust} was related to the gas density by the dust-to-gas ratio. The dust parameters were chosen with the assumption of that the dust was silicate dust. B_ν is the black body function. The local mean radiation field was retrieved from integrating the intensity over all solid angles,

$$J_\nu = (4\pi)^{-1} \int I_\nu d\Omega. \quad (3.11)$$

The mean radiation field was used together with the collisional excitation or de-excitation rate C_{il} , between two states, i and l , to calculate the state population [26]

$$n_i = \frac{\sum_{l>i} n_l A_{li} + \sum_{l\neq i} n_l (B_{li} J_{li} + C_{li})}{\sum_{l<i} A_{il} + \sum_{l\neq i} (B_{il} J_{il} + C_{il})}, C_{il} = \frac{g_l}{g_i} c_{il} e^{\frac{-hc}{k_B T_{gas}} (E_l - E_i)}. \quad (3.12)$$

The statistical weights, g_l and g_i , and the rate coefficients, c_{il} , are input parameters in the model when calculating, C_{il} . The constants in the equations are the Boltzmann constant, k_B , and the light speed in vacuum, c .

The Equations (3.8), (3.9), (3.11) and (3.12) create a recursive problems serving as a baseline for the LIME code. The LIME code also accounts for Doppler shifts between different regions of the envelope.

4

Results

Two scenarios were modelled. An explosion scenario, where all the matter is ejected simultaneously and a scenario with an outflow with an ejection velocity that decreased with time. While the outflow in both scenarios started close to the central star, the profiles were modelled in the outer shell. The outer shell is the cold region in the Boomerang Nebula ranging from $r_{in} = 8.7 \times 10^3$ AU ($6''$) to $r_{out} = 48 \times 10^3$ AU ($33''$), see Figure 1.3.

From the stellar wind models radial profiles of velocity, density and temperature were calculated. These were input into a radiative transfer (RT) model to create image cubes. CASA, the Common Astronomy Software Applications package, was used to extract the CO($J = 1 - 0$) line shapes from the image cubes. The line shapes were calculated from two circular apertures, with radii $r_1 = 3''$ and $r_2 = 30''$. These apertures can be compared to the ALMA data and the SEST data, respectively. The smaller aperture provides the line of sight absorption, where the larger aperture grants us the total velocity dispersion in the Nebula.

Initially, the models included an earlier slow AGB wind to be swept up by the ejection. The slow wind was given a velocity of 15 km/s and a mass loss rate rate $10^{-5} M_{\odot}/\text{year}$, based on typical parameters for the outflow from AGB stars. Figure 4.1 shows how the density would behave with the presence of an AGB wind in the explosion scenario. When the fast ejecta collides with the AGB wind, the velocity at the wind front decreases. As the AGB wind gets swept up, a density peak is formed at the wind front (see Figure 4.1). The observation does not show any signs of shock features.

Another argument for there being no traces of the previous AGB wind inside the cold shell is that it is too slow to cool adiabatically. An AGB wind would have a temperature higher than the CMBR (see Figure 4.2). At low velocities the adiabatic cooling is too weak to counterbalance the photoelectric effect, so such an AGB wind can not absorb against the CMBR. Figure 4.3 shows spectra at different times with an explosive wind colliding with an AGB wind. Before 1150 years, the constant AGB wind is still present in the shell, appearing as a thin line at low velocities. This feature is missing from the observations. Hence, the AGB wind needs to have a very low mass loss rate, leading to a very small effect on the fast ejecta. Another possible scenario is that the previous AGB wind already has left the shell and have dissociated or heated up to the background temperature.

As Figure 4.3 shows the spectra depends on the life time of the Nebula, but it was not treated as a free parameter. The gas at r_{out} may still be colder than the CMBR, so it was assumed that the fast-velocity ejected gas just filled the shell. In the velocity decrease scenario, this happens when the fastest mass bin reaches r_{out} . For

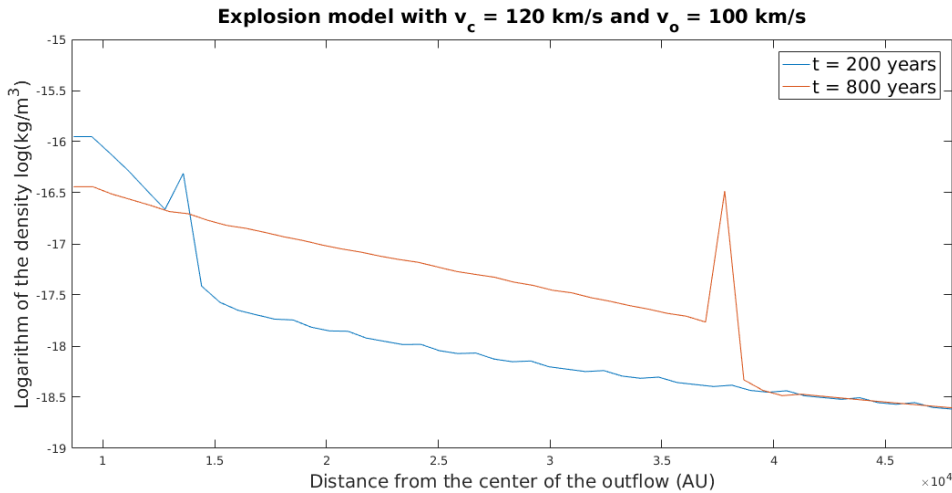


Figure 4.1: The logarithm of the density for an explosion model. The explosion used the parameters $v_c = 120$ km/s and $v_o = 100$ km/s (see Equation (3.3)). The total gas mass is $M = 2.9M_\odot$. The model includes an AGB wind moving at a velocity of 15 km/s and has a mass loss rate of $\dot{M} \approx 10^{-5}M_\odot/\text{year}$.

the explosion scenario, however, this time is not always straight-forward to define, see discussion below.

4.1 Explosion scenario

Technically the shell is full when the fastest mass bin reaches r_{out} . But in the case of a Gaussian velocity distribution, the maximum velocity depends on the amount of the mass bins. Hypothetically, if our simulation used an infinite amount of mass bins, the maximum velocity would also be infinite. But the fraction of mass bins at high velocities are very low, see Figure 4.4, so the density at the edge of the shell would be too low to significantly affect the line shape. Instead, what was chosen was

$$t = r_{out}/(v_c + 2v_o). \quad (4.1)$$

At this time only $\approx 2.5\%$ of the total mass has passed r_{out} . Meanwhile, as seen in 4.4, a significant fraction of the mass bins has passed r_{in} , so that most of the mass from the explosion has reached the outer shell.

On the one hand, the velocity profile was independent of the parameters of the initial velocity distribution, since an instant ejection generates a linear velocity profile

$$v = r/t. \quad (4.2)$$

On the other hand, the density profile depends significantly on the parameters of the initial velocity distribution. Figure 4.5 shows how the density profile changes with

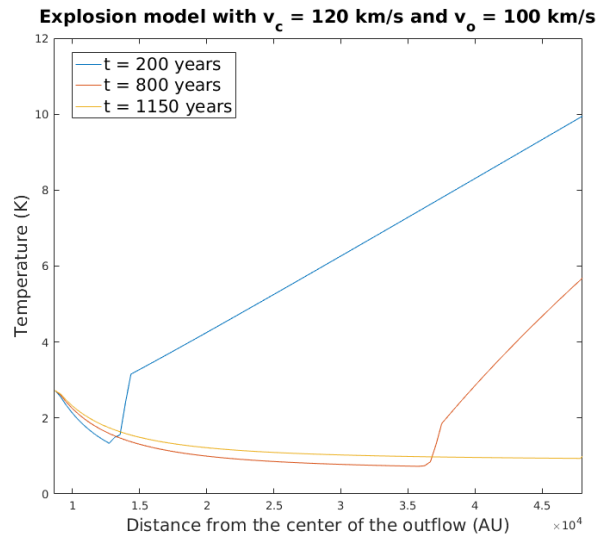


Figure 4.2: The temperature profile for an explosive wind colliding with an AGB wind. The explosion uses the parameters $v_c = 120 \text{ km/s}$ and $v_o = 100 \text{ km/s}$ (see Equation (3.3)) and the total gas mass is $1.4 M_\odot$. The AGB wind has a velocity at 15 km/s and a mass loss rate of $\dot{M} \approx 10^{-5} M_\odot/\text{year}$.

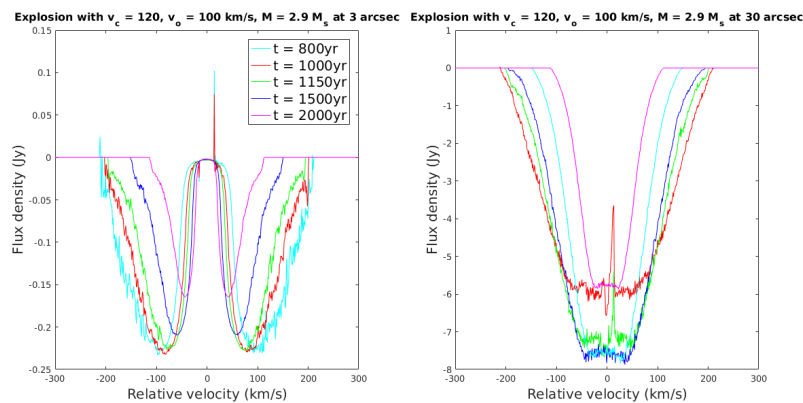


Figure 4.3: Spectra for an explosion scenario model with an AGB wind, at different times. The explosion model has parameters $v_c = 120 \text{ km/s}$ and $v_o = 100 \text{ km/s}$ (see Equation (3.3)) and a total mass of $2.9 M_\odot$. The AGB wind is moving at a constant velocity of 15 km/s and had a mass loss rate of $10^{-5} M_\odot/\text{year}$. After 1150 years, the AGB wind has left the shell.

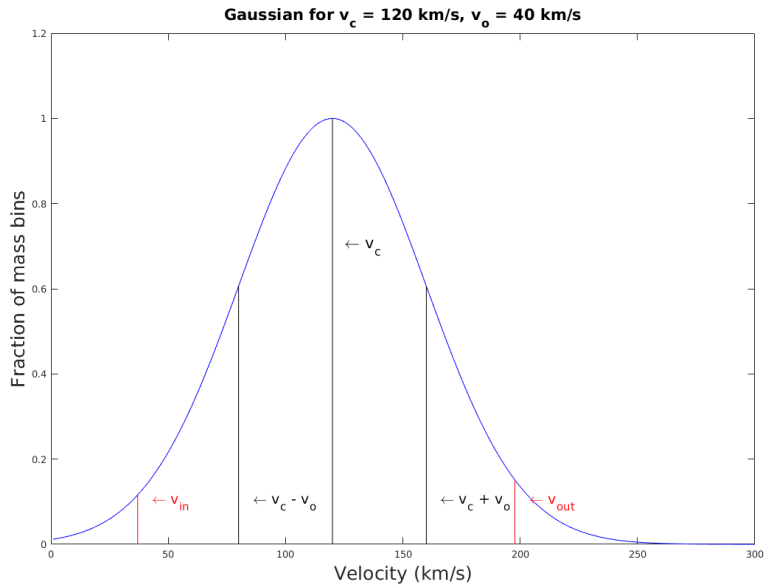


Figure 4.4: The Gaussian distribution of an explosion with $v_c = 120$ km/s and $v_o = 40$ km/s. The velocity at the outer edge of the cold shell is $v_{out} = v_c + 2v_o$ and the velocity at its inner edge is v_{in} . At this time, most of the mass from the explosion is inside the shell.

the velocity parameters and the total gas mass M . The smaller v_o in comparison to v_c , the more apparent is the effect of the initial velocity distribution. It appears as a bulge compared to the constant velocity density, $\rho \propto r^{-2}$. But when v_o is large compared to v_c , v_c has little effect on the density. The total gas mass, M , only serves as a scaling parameter for the density.

As seen in figure 4.7, the dominant heating effect in the outflow is the photoelectric heating. Equations (2.5) and (2.9) states how its effect on the temperature is inversely proportional to v . Since the main component of the adiabatic cooling (see Equation (2.5)) only depends on r , Figure 4.6 shows how the temperature approaches $T \propto r^{-4/3}$, the case with only adiabatic cooling, as the outflow velocity, v_c or v_o , increases. The temperature varies very little with the gas mass M , since the density dependent heating factors in Figure 4.7 have little impact on the outflow temperature.

The radiative transfer (RT) software created intensity image cubes from the radial profiles, containing absorption intensity for different observations angles and velocities. The spatial dependence of the absorption from an explosion model can be seen in Figure 4.8. The Doppler effect states that to see gas moving at a specific velocity, we need to look at it with a certain frequency.

CASA was used to produce the CO($J = 1 - 0$) line shape from the image cube. It was investigated how the parameters changed the line shape. The impact of altering v_c depended on it how it compares to v_o . When v_o was large compared to v_c , the line

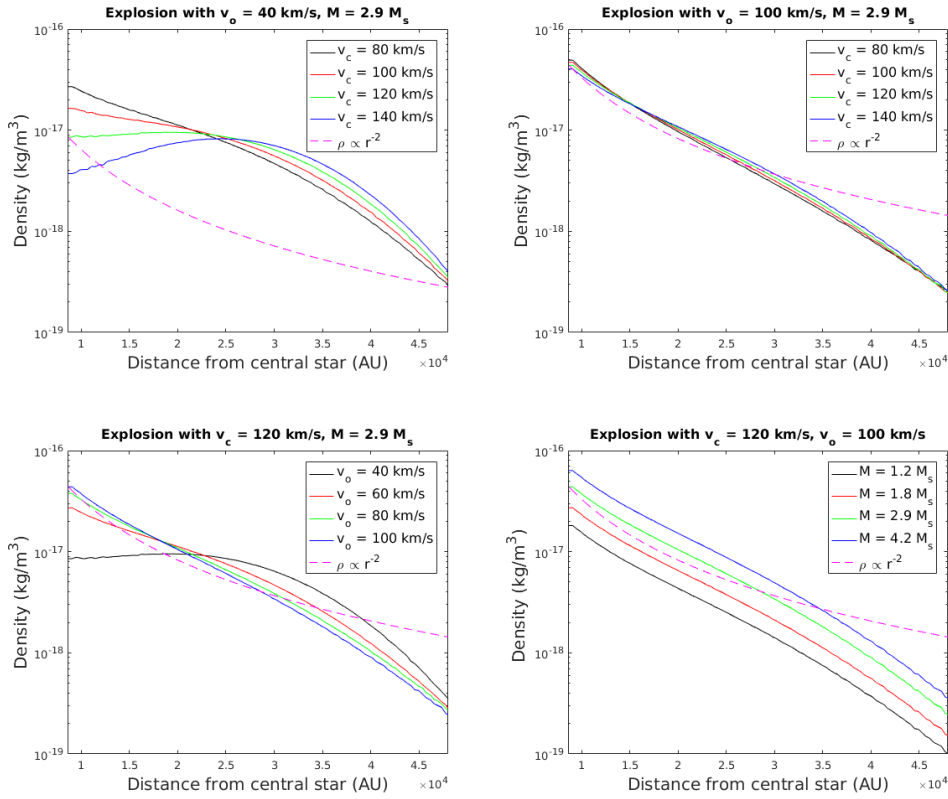


Figure 4.5: The density profile for different parameters in the explosion scenario. The time is chosen accordingly to Equation (4.1). The profiles are compared to $\rho \propto r^{-2}$, the density profile for a constant wind velocity.

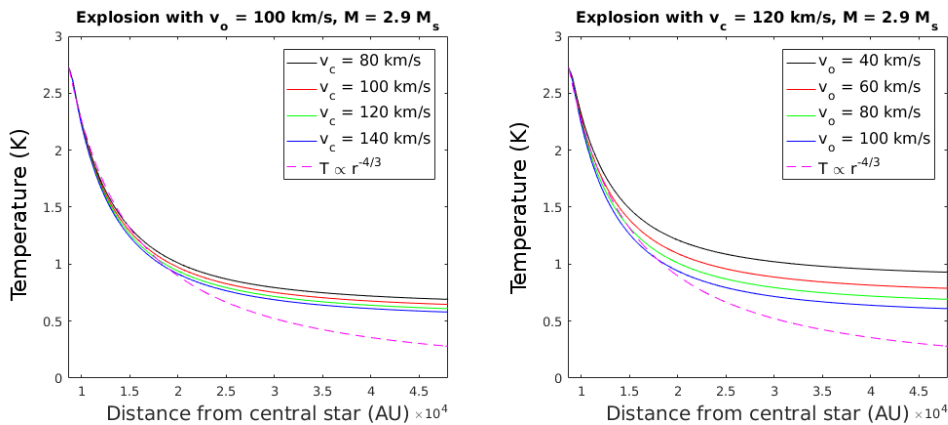


Figure 4.6: The temperature profile for different velocity parameters, v_o and v_c , in the explosion model. The time is chosen accordingly to Equation (4.1). The temperature asymptotes $T \propto r^{-4/3}$, the case of constant velocity without molecular heating, as the outflow velocity increases and the photoelectric heating weakens.

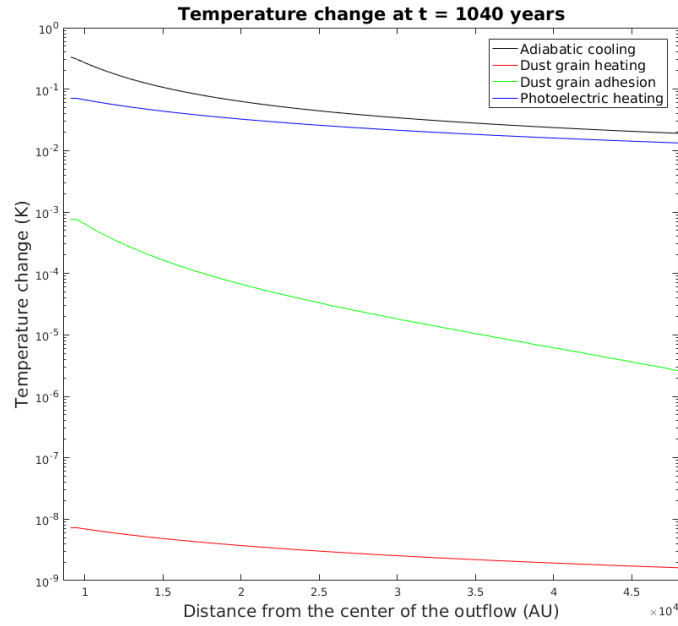


Figure 4.7: The absolute value of the different heating and cooling mechanisms in the explosion scenario, 1040 years after the initial explosion. The parameters $v_c = 100$ km/s and $v_o = 60$ km/s, see Equation (3.3). The total gas mass in the explosion is $1.4M_\odot$.

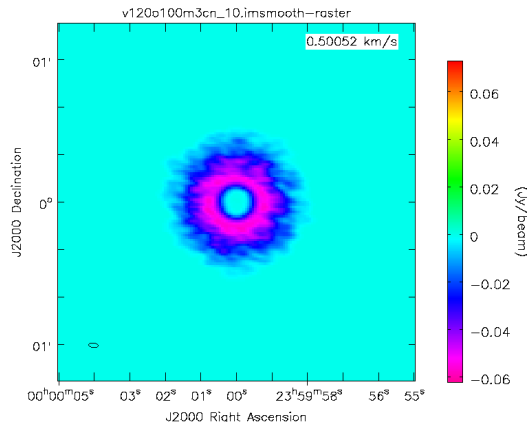


Figure 4.8: The intensity map of an outflow with the explosion scenario, 1150 years after the initial explosion. The parameters $v_c = 220$ km/s and $v_o = 120$ km/s, see Equation (3.3). The total gas mass in the explosion is $2.9M_\odot$. The color map is for velocities at $v = 0.5$ km/s

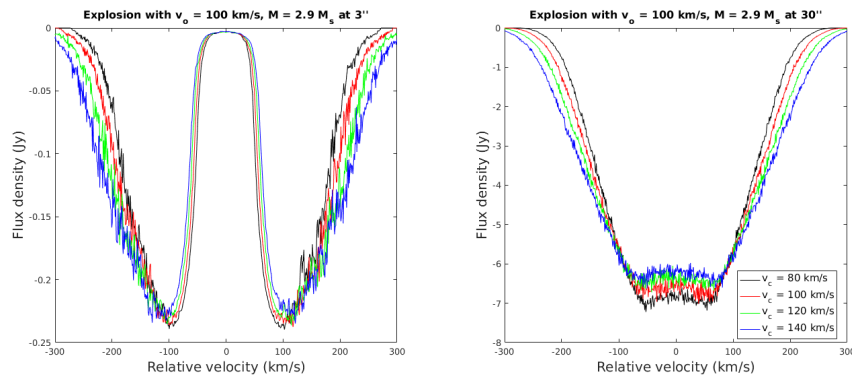


Figure 4.9: Spectra from the explosion scenario, for different values of v_c . The total gas mass is $M = 2.9M_\odot$. The offset velocity is $v_o = 100$ km/s.

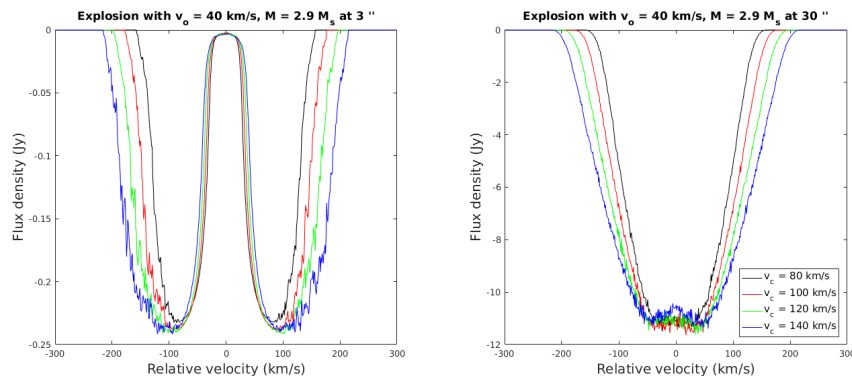


Figure 4.10: Spectra from the explosion scenario for different values of v_c . The total gas mass is $M = 2.9M_\odot$. The offset velocity is $v_o = 40$ km/s.

shapes' wings grew wider. But when v_o was smaller, there were also visible changes in the velocity dispersion with maximal absorption. (See Figure 4.9). For small v_o the inner part of the cold region will be less dense, and the density distribution depends more on v_c .

Varying v_o gave similar effects. The wings widened, as well as the maximum absorption velocity range (see Figure 4.11). The absorption intensity also decreases with v_o , as large v_o has a smaller density (See Figure 4.5).

The absorption intensity increases with M . As discussed before, this parameter is a scaling factor for the density. As the outflow grows denser, the more it absorbs the CMBR. Other line shape features vary little with M , so M serves not only as scaling factor for the density, but also for the line shape.

In the larger aperture, it was possible to fit the ALMA+SEST data with an explosion model, with $v_c = 120$ km/s and $v_o = 100$ km/s (see Figure 4.13). However, neither of the parameters had large effects on the model spectrum in the smaller aperture. It is also not possible to find a good fit to the line shape in the small aperture.

4. Results

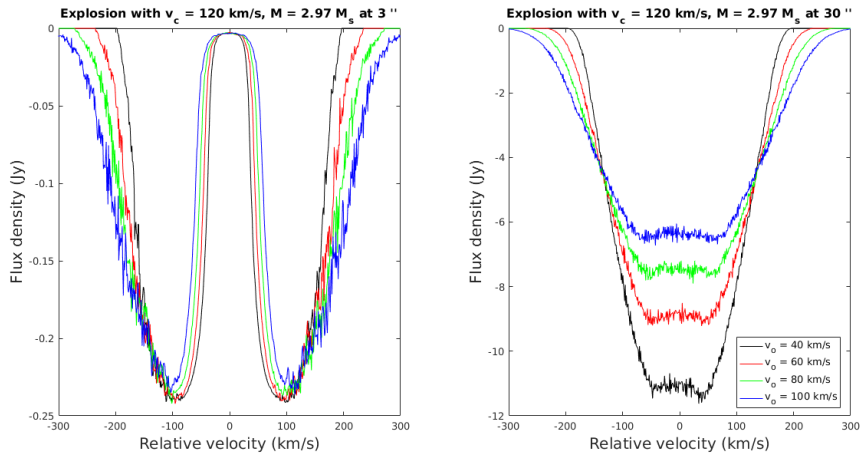


Figure 4.11: Spectra from the explosion scenario for different values of v_o . The total gas mass is $M = 2.9M_\odot$. The central velocity is $v_c = 120$ km/s.

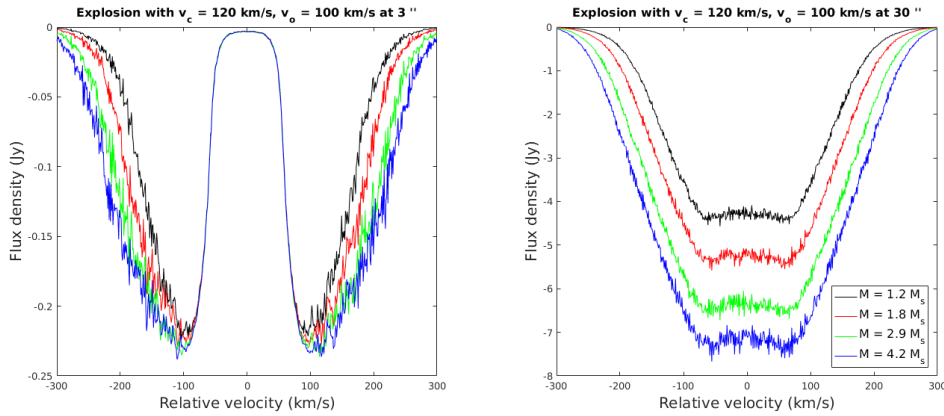


Figure 4.12: Spectra from the explosion scenario for different gas mass M . The central velocity is $v_c = 120$ km/s and the offset velocity is $v_o = 100$ km/s.

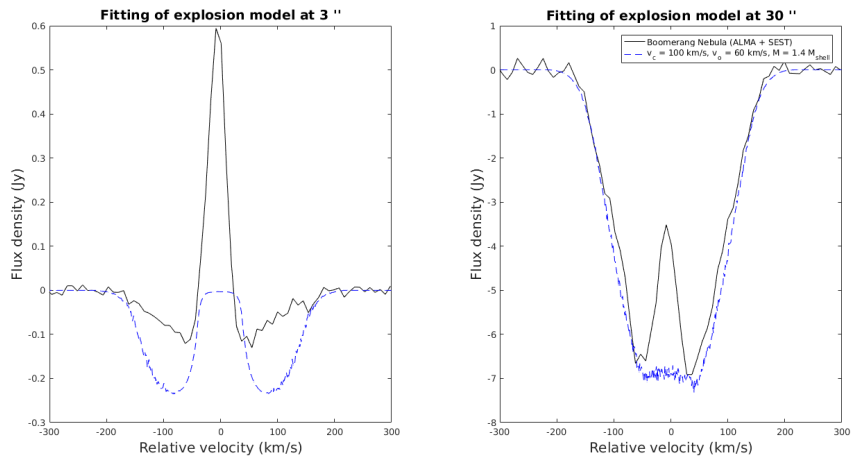


Figure 4.13: The best fit of the explosion scenario to the SEST+ALMA data. This model has $v_c = 120$ km/s, $v_o = 100$ km/s and $M = 1.8M_\odot$.

4.2 Decreasing velocity scenario

In the first scenario all the mass was ejected instantly with a velocity distribution, while in the second scenario it was ejected continuously with an ejection velocity decreasing over time. A velocity increase would clump the ejecta together into a single wind front. This deviates from the observations, and is thus not considered in the models.

The decreasing velocity scenario was modelled with a power law

$$v(r = 0, t) = v_i \left(\frac{t}{t_i}\right)^{-\alpha}, \quad (4.3)$$

where the power law coefficient was limited to $\alpha > 0$. The outflow starts at $t_i = 1$ year with an initial velocity, v_i .

When α is high, v approaches a linear behavior (See 4.14). This can be confirmed analytically. The distance a particle which has been released at a time, t_r , and a velocity, v has moved is

$$r = v(0, t_r)(t - t_r), \quad (4.4)$$

where $t = r_{out}/v_i$ is the time when the gas has filled the shell. By substituting this and $v(0, t_r)$ from Equation (4.3), as well as dividing with r_{out} ,

$$\frac{r}{r_{out}} = \frac{v_i t}{r_{out}} \left(\frac{t_r}{t_i}\right)^{-\alpha} - \frac{v_i t_r}{r_{out}} \left(\frac{t_r}{t_i}\right)^{-\alpha} = \frac{v}{v_i} \left(1 - \frac{t_r}{t}\right). \quad (4.5)$$

This means that if $t_r \ll t$, v is linear to r . This is equivalent to the gas being ejected during a short interval, corresponding to a large α . With a small α , the velocity change is less drastic and the gas in the shell has been ejected during a longer time. This is equivalent to the behavior in Figure 4.14.

The non-linearity of the velocity profile is reflected in the density profile. Figure 4.15 shows that the profile turns from concave to convex as α increases. The figure also shows that the curves are much steeper than those a constant velocity model. It is steepest around $\alpha \approx 0.2$, where $\rho \propto r^{-4.5}$. Meanwhile the minimum declination in the interval is $\rho \propto r^{-3}$.

The temperature is independent of α for models with a linear velocity profile ($\alpha \geq 0.4$) (see Figure 4.16). Similar to the explosion scenario (see Figure 4.6), the temperature profile approaches $T \propto r^{-4/3}$, for large v_i . As shown in 4.17, this is again from the photoelectric heating (see end of 4.1). Due to the radial dependence in the adiabatic cooling, it asymptotically approaches the photoelectric heating at high radii (see Equation (2.5)).

Based on these profiles, LIME was used to calculate the line shapes for the decreasing velocity scenario [26]. Figure 4.18 shows spectra with different values of α . Here α was varied between 0.1 and 1.2. As α increased, the velocity dispersion in the

4. Results

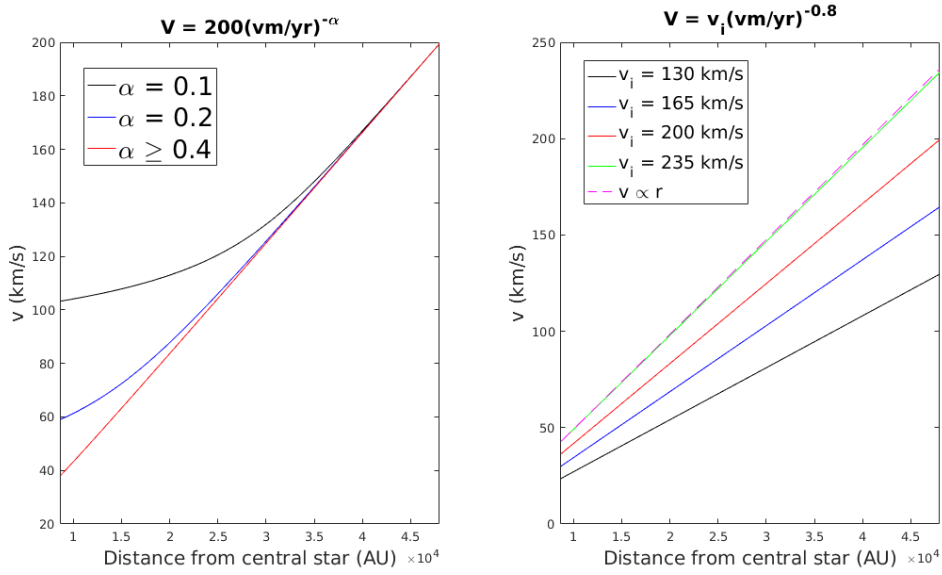


Figure 4.14: The radial velocity profile for different ejection velocity parameters, v_i and α . As α increases, the velocity profile becomes linear.

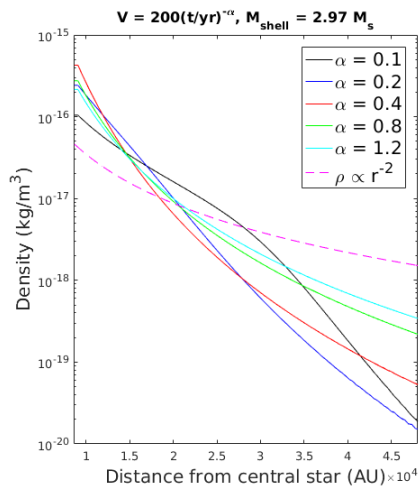


Figure 4.15: The radial density profile for different ejection velocity parameters, v_i and α . The density is much steeper than a constant velocity model.

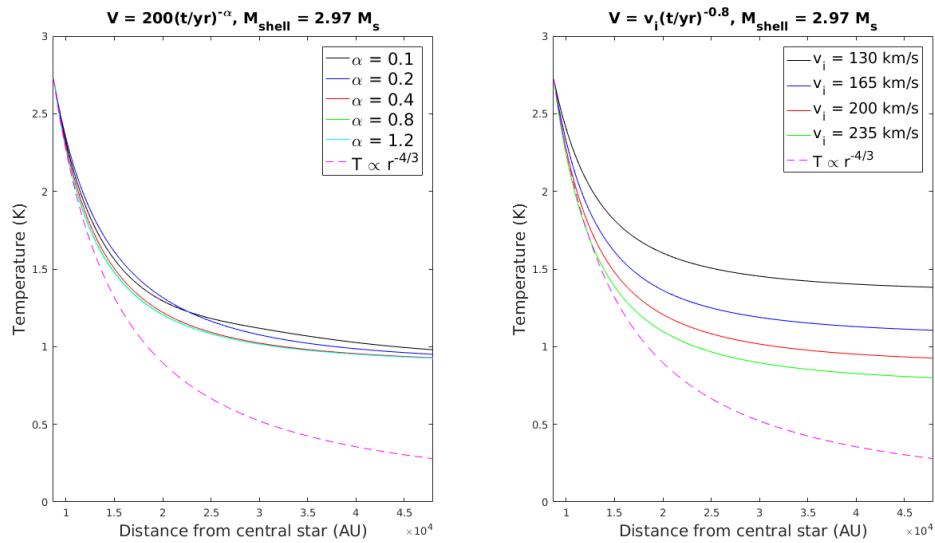


Figure 4.16: The radial temperature profile for different ejection velocity parameters, v_i and α . The temperature approaches $T \propto r^{-4/3}$, when v_i increases, which is the case of a constant velocity and no heating.

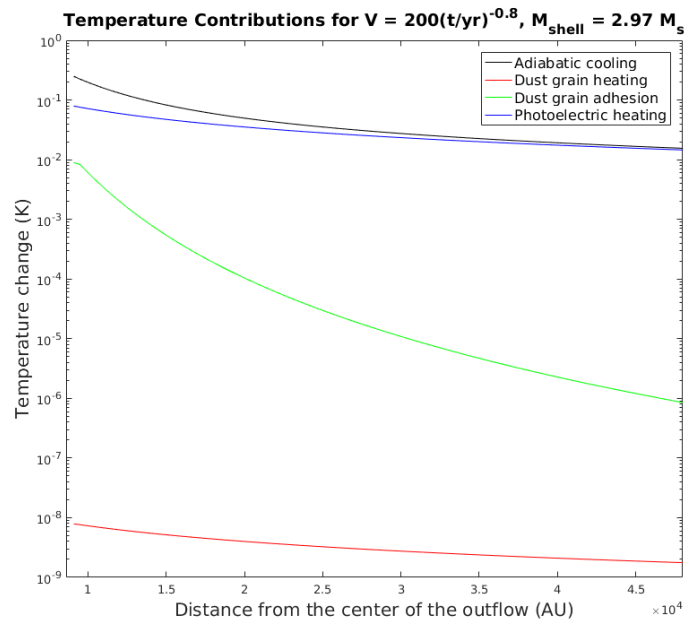


Figure 4.17: The absolute value of the heating and cooling mechanisms in the decreasing model, with $t = 1388$ years and $v(r = 0, t) = 165 * t^{-0.5}$ km/s. The dominant heating factor is the photoelectric heating, just weaker than the adiabatic cooling.

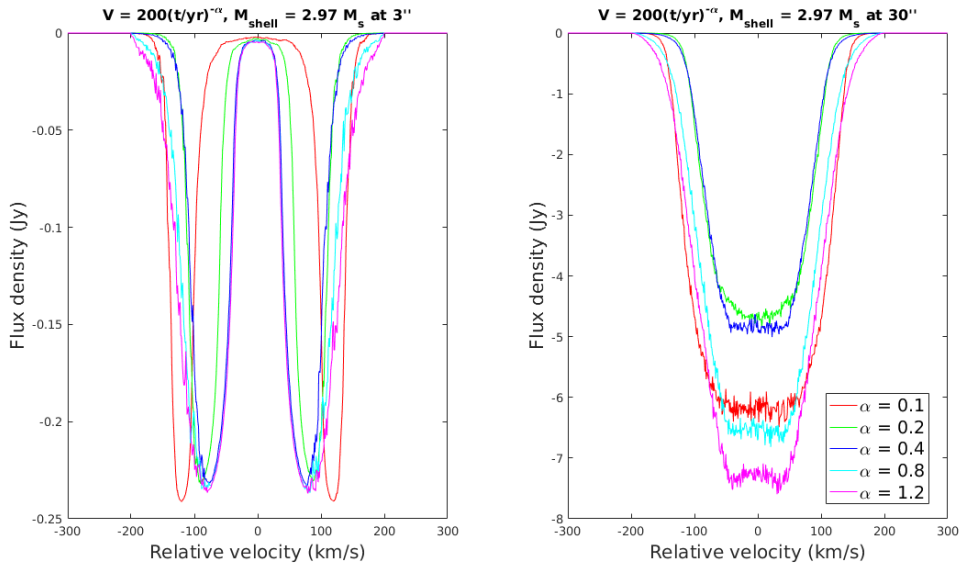


Figure 4.18: The spectra of $v(r = 0, t) = 165(t/\text{year})^{-\alpha}$ km/s, where α is varied between 0.1 and 1. The spectra are taken when the front of the gas reaches the outer edge of the outer shell.

large aperture decreased, causing the line to become narrower. For a higher α , the velocity dispersion is larger within the shell.

In the small aperture, the spectra widened with α , and for $\alpha > 0.2$, the absorption at low velocities vanished. The velocity changed so slowly within the shell, that the line shapes resemble the constant velocity model in Figure 3.2.

The absorption intensity changes very little with α . However, Figure 4.19 shows that it increases with v_i , when the photoelectric heating weakens. Meanwhile the velocity peak moves outward, as the velocity distribution in the shell increases.

In the large aperture the line width increases for a high v_i , due to Doppler line broadening. Meanwhile as the absorption is spread out over more velocities, the absorption peak decreases.

Finally, figure 4.20 shows that the shell mass has a similar role as the total gas mass in in the explosion scenario (See 4.12).

The best decreasing velocity model had an ejection velocity, $v(r = 0) = 200(t/\text{year})^{-0.8}$ km/s, and a shell mass, $2.97M_{\odot}$. It fitted the SEST+ALMA data in the $R < 30''$ region, but looked the same as the explosion scenarios in the inner region (see Figure 4.21). The spectrum for this inner region changed little with the parameters and had a different shape from the SEST+ALMA data.

4.3 Considering a large shell size

Since neither of the scenarios provides an accurate fit for both the apertures, alternatives for improving the fits were investigated. A parameter that was particularly successful in improving the model fits was the size of the outer shell. In the models discussed up to this point, the shell size was assumed to be that given by Sahai et

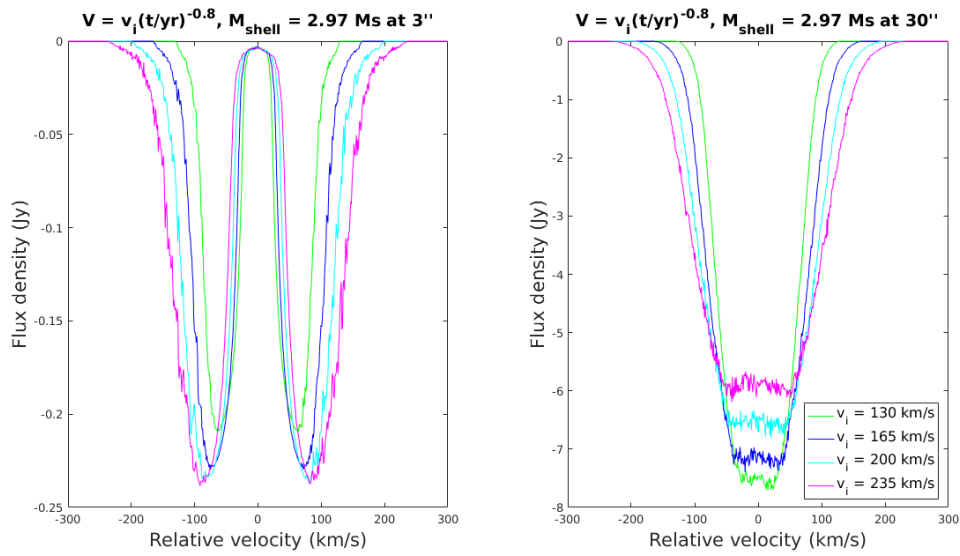


Figure 4.19: The spectra of $v(r = 0) = v_i(t/\text{year})^{-0.8}$, where v_i is varied. The spectra are taken when the front of the gas reaches the outer edge of the outer shell.

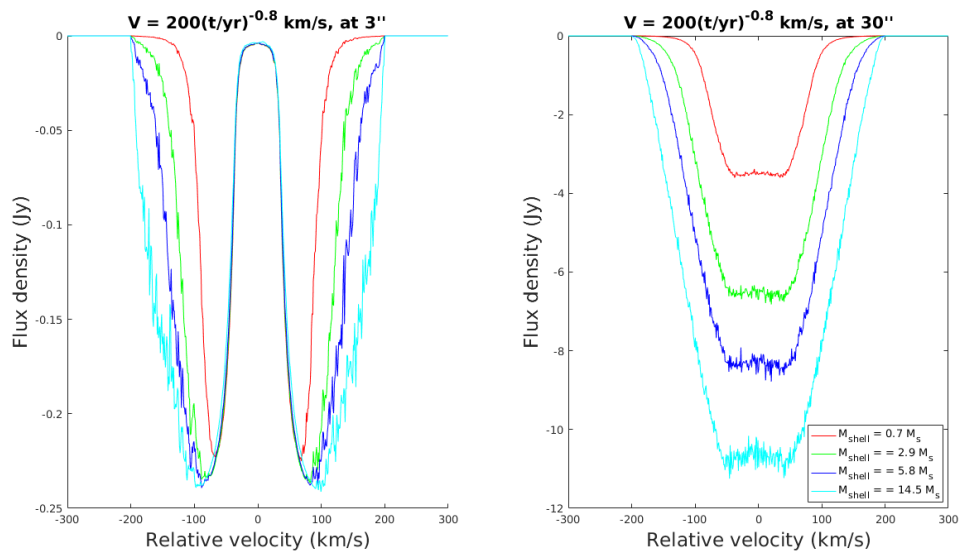


Figure 4.20: The spectra of $v(r = 0) = 200(t/\text{year})^{-0.8} \text{ km/s}$, where the shell mass is varied. The spectra are taken when the front of the gas reaches the outer edge of the outer shell.

4. Results

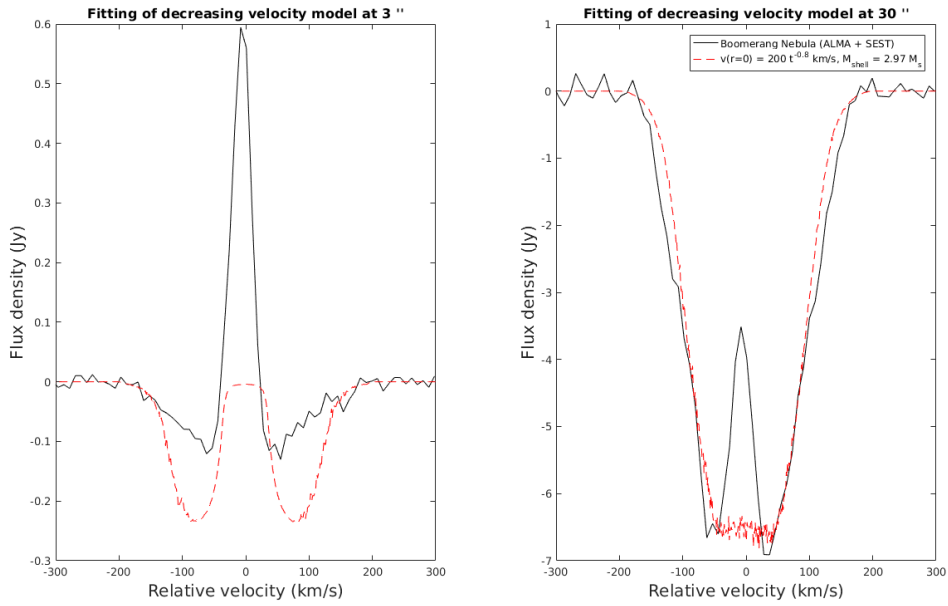


Figure 4.21: The best fit for the decreasing wind scenario to the SEST+ALMA data. The ejection velocity is $v(r = 0) = 200(t/\text{year})^{-0.8}$ km/s and a shell mass $2.97M_{\odot}$.

al. [5], but by increasing the model's outer radius, the fit to the spectrum from the $3''$ can be greatly improved. Figure 4.22 shows a model with an outer shell radius of $75''$ instead of $32''$. The model shown is an explosion model with parameters $v_c = 160$ km/s, $v_o = 60$ km/s and $M = 2.97M_{\odot}$, and is able to fit both spectra better than the models discussed previously. This result indicates that the region in the Boomerang Nebula that absorbs the CMBR might be considerably larger than previously thought. Although investigating this issue further is outside of the scope of this thesis, this is an important finding that requires further investigation.

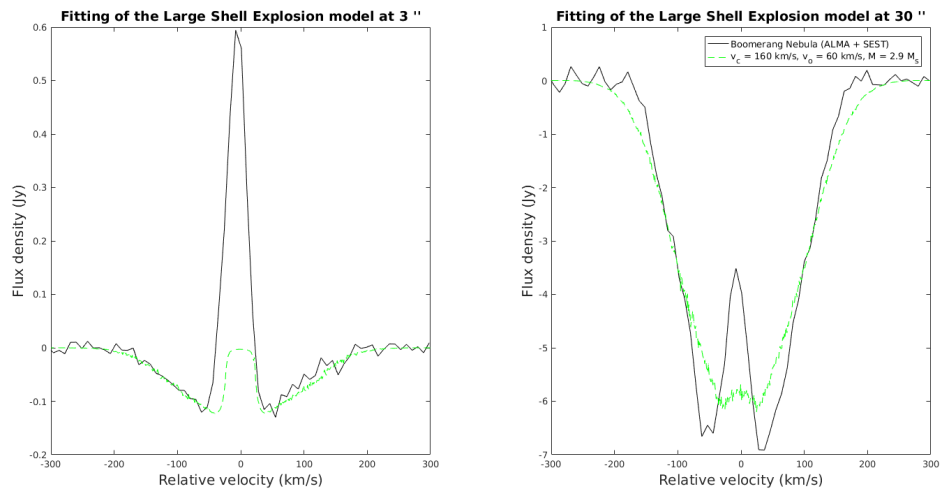


Figure 4.22: The fit of an explosion model where the outer shell has a radius $75''$. The velocity parameters are $v_c = 160$ km/s and $v_o = 60$ km/s. The total gas mass in the ejection is $2.9M_\odot$.

5

Conclusion

The aim of this thesis was to determine how the cold outflow was ejected. We were not able to conclude on which of this two scenarios is better to explain the Boomerang Nebula, however the result presented here can be used to set limits for the free parameters and better understand their impact on the spectrum. The best decreasing velocity model was ejected during a short time, almost like an explosion model.

5.1 Interpretation of Results

The best explosion model had a velocity distribution with the parameters $v_c = 100$ km/s and $v_o = 60$ km/s (see Equation (3.3)) and a total gas mass $1.4M_\odot$. The best decreasing velocity model had an ejection velocity $v(r = 0, t) = 200(t/\text{year})^{-0.8}$ and a shell mass $2.97M_\odot$. Figure 5.1 shows the spectra for the two best models. Both scenarios are able to provide good estimates in a $30''$ aperture, and while they look similar in the $3''$ aperture, they are unable to fit the observations and changes little with their parameters.

Even if their spectra are so similar in both apertures, the circumstellar envelopes have significantly different characteristics (see Figure 5.2). Their temperature profiles looks similar, but the explosion model shows higher velocities and lower densities than the decreasing velocity model.

5.2 Wind mechanism

The mechanism accelerating the outflow is unknown. Generally stellar winds are accelerated by radiation pressure, but the winds of several biconal preplanetary nebulae have too high linear momentum and energy to be supplied solely by radiation pressure. The linear momentum of our wind models can be calculated as

$$P = \int_{r_{in}}^{r_{out}} \rho(r)v(r)4\pi r^2 dr. \quad (5.1)$$

and the kinetic energy in the outflow from

$$E_{kin} = \frac{1}{2} \int_{r_{in}}^{r_{out}} \rho(r)(v(r))^2 4\pi r^2 dr. \quad (5.2)$$

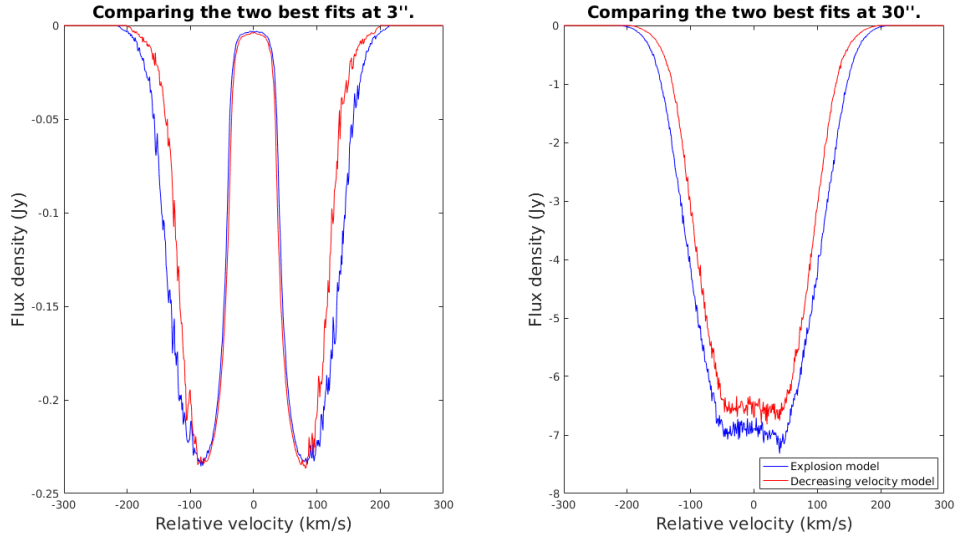


Figure 5.1: The spectra from the two scenarios' best models. The explosion model was ejected instantly with a Gaussian velocity distribution with the central velocity, $v_c = 100$ km/s and the velocity offset, $v_o = 60$ km/s. The total mass in the explosion was $1.4M_\odot$. The time decrease model used an ejection velocity $v(r = 0, t) = 200(t/\text{year})^{(-0.8)}$ and a shell mass $2.97M_\odot$.

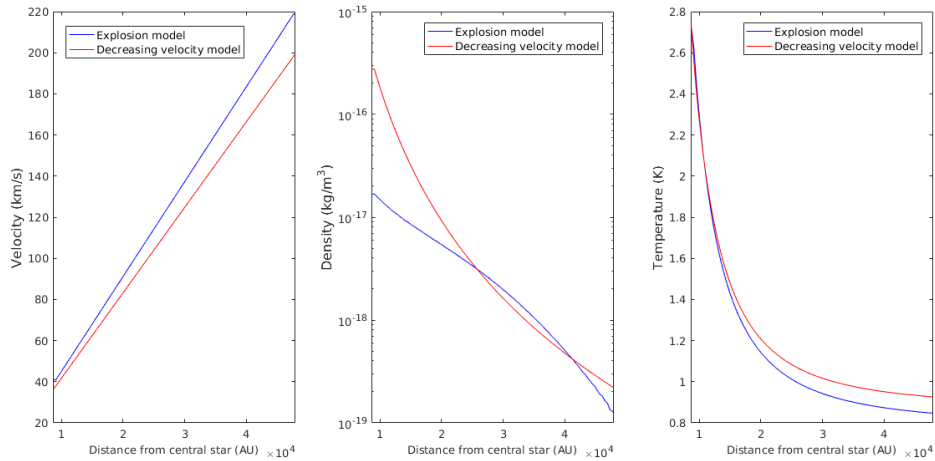


Figure 5.2: The velocity, density and temperature profiles from the two scenarios' best models. The explosion model was ejected instantly with a Gaussian velocity distribution with the central velocity, $v_c = 100$ km/s and the velocity offset, $v_o = 60$ km/s. The total mass in the explosion was $1.4M_\odot$. The time decrease model used an ejection velocity $v(r = 0, t) = 200(t/\text{year})^{(-0.8)}$ and a shell mass $2.97M_\odot$.

The best-fitting explosion model (see Figure 5.1) has a total linear momentum, $P = 2.78 \times 10^{35}$ kgm/s. Sahai and Nyman [4] calculate a luminosity, $L = 300L_{\odot} = 1.154 \times 10^{29}$ J/s, for the central star of the Boomerang Nebula. While the star is very luminous, it would take the wind $P/(L/c) = 2.3 \times 10^7$ years to reach this momentum, if radiation pressure was the driving force of the wind. This is usually assumed to be the case for evolved stars, but would not be possible for the Boomerang Nebula because the explosion model predicts an outflow which is only 1030 years old.

Similar results are shown from the best-fitting velocity decrease model (see Figure 5.1). Its linear momentum 4.46×10^{35} kgm/s indicates a required lifetime of 3.7×10^7 years, several orders of magnitude larger than the modelled lifetime of 1143 years. This means that some other unknown wind mechanism has accelerated the outflow. Another possible mechanism behind the wind acceleration is an energy transfer from a binary companion. If the companion migrates inwards, the gravitational energy stored in the orbit will be released. The gravitational energy, E_g , is given from integrating the gravitational potential from infinity to the radius at which the inwards migration ends, R_f . The gravitational potential is

$$F_g = -\frac{GM_s M_c}{r^2}, \quad (5.3)$$

where r is the distance between the binary stars, M_s the mass of the absorber and M_c the mass of its companion. Integrating the gravitational potential gives the gravitational energy

$$E_g = -\int_{\infty}^{R_f} \frac{GM_s M_c}{r^2} = \frac{GM_s M_c}{R_f}. \quad (5.4)$$

The masses of the two stars are poorly constrained, but since the models predict an envelope with a mass between $1.4M_{\odot}$ and $2.97M_{\odot}$, it is assumed that the primary star has a mass of $3M_{\odot}$. The mass of the companion is certainly lower than that of the primary and it is assumed to be $1M_{\odot}$. This gives a gravitational energy

$$E_g = \frac{5.292 \times 10^{39}}{R_f(\text{AU})}. \quad (5.5)$$

Equation (5.2) gives a kinetic energy, $E_k = 1.8 \times 10^{40}$ J for the best-fitting explosion model and $E_k = 2 \times 10^{40}$ J for the best-fitting decreasing velocity model. The primary star in a binary source tends to be an AGB star, with a stellar radius of roughly one AU [2]. Meanwhile the explosion (decreasing velocity) model provides an upper limit, for conversion from gravitational energy to kinetic energy, at $R_s < 0.29$ AU ($R_s < 0.26$ AU). This would be smaller than the expected radius of the AGB primary star and, hence, the stars would be expected to merge before releasing enough energy to accelerate the outflow. Since the parameters of the binary pair are very uncertain and the physics of outflow ejection in this scenario is not well understood, it is not possible to draw strong conclusions on this matter.

6

Future Prospects

The result from this thesis is not conclusive, but it sets important constraints on the shortcomings of the simple scenarios considered. And while it gives a hint of the origin of the Nebula, further studies are needed to draw stronger conclusions. The models presented here can be improved in several ways. An example is allowing the mass-loss rate to vary in the decreasing velocity scenario. Similarly, in the explosion scenario the mass of the mass bins could vary based on their velocity.

It would be interesting to investigate the large shell model shown in Figure 4.22 more thoroughly. Even if the Boomerang Nebula is not larger than assumed, the model might help improve the simulations. It would also be interesting to research the spectra's parameter dependence in a larger shell to improve the fit.

To further constrain the model more molecular lines could be used. The $\text{CO}(J = 2 - 1)$ line was also modeled, but due to a low signal-to-noise rate the comparison deemed to be too inconclusive. More extensive data in general could help the modelling of the Nebula. For example, atomic lines could shed light on the dissociation of a previous AGB wind

There are other parts of the Boomerang Nebula that need more extensive modelling. The dust of the Nebula is not modelled extensively. By understanding the other aspects of the nebulae, one of the two scenarios might be disproved. More extensive modelling and new observation can also aid with setting further constraints on the free parameters.

Bibliography

- [1] Arnab Rai Choudhuri. *Astrophysics for physicists*. Cambridge University Press, 2010.
- [2] H. J. Habing and Hans Olofsson. *Asymptotic giant branch stars*. Springer, 2004.
- [3] Robert Hollow. Post-main sequence stars, 2002.
- [4] Raghvendra Sahai and Lars-Åke Nyman. The boomerang nebula: The coldest region of the universe? *The Astrophysical Journal*, 487(2), Jan 1997.
- [5] R. Sahai, W. H. T. Vlemmings, P. J. Huggins, L.-Å. Nyman, and I. Gonidakis. Alma observations of the coldest place in the universe: The boomerang nebula. *ApJ The Astrophysical Journal*, 777(2):92, 2013.
- [6] Bruce T. Draine. *Physics of the interstellar and intergalactic medium*. Princeton University Press, 2011.
- [7] Cool cosmos.
- [8] Richard B Larson. The physics of star formation. *Reports on Progress in Physics*, 66(10):1651–1697, Oct 2003.
- [9] Robert Hollow. Post-main sequence stars, 2002.
- [10] Richard A. Shaw. Shape, structure, and morphology in planetary nebulae. *Proceedings of the International Astronomical Union*, 7(S283):156–163, 2011.
- [11] Kenneth R. Lang. *Essential astrophysics*. Springer, 2013.
- [12] Richard W. Pogge. The fate of massive stars, Aug 2016.
- [13] G. Wegner and I. S. Glass. A new bipolar nebula in centaurus. *Monthly Notices of the Royal Astronomical Society*, 188(2):327–330, Jan 1979.
- [14] V. Bujarrabal, A. Castro-Carrizo, J. Alcolea, and C. Sánchez Contreras. Mass, linear momentum and kinetic energy of bipolar flows in protoplanetary nebulae. *Astronomy & Astrophysics A&A*, 377(3):868–897, 2001.
- [15] Brian H. Bransden and Charles J. Joachain. *Physics of atoms and molecules*. Prentice Hall, 2010.
- [16] Eugene Hecht. *Optics*. Addison-Wesley, 2002.
- [17] ESO. Swedish-eso submillimetre telescope (decommissioned).
- [18] Alejandro Peredo. Alma.
- [19] Stan Owocki. Stellar winds. *Planets, Stars and Stellar Systems*, page 735–788, 2013.
- [20] P. Goldreich and N. Scoville. Oh-ir stars. i - physical properties of circumstellar envelopes. *ApJ ApJL The Astrophysical Journal*, 205:144, 1976.
- [21] Daniel V. Schroeder. *An introduction to thermal physics*. Addison Wesley, 2000.
- [22] T. Danilovich. *Mass loss and molecules: Studies of galactic AGB stars*. Chalmers University of Technology, 2016.

- [23] Martin Groenewegen. The circumstellar shells of carbon miras. *Circumstellar Matter 1994*, page 321–324, 1995.
- [24] P. J. Huggins, H. Olofsson, and L. E. B. Johansson. The CO envelope of IRC +10216. *apj*, 332:1009–1018, September 1988.
- [25] G. A. Mamon, A. E. Glassgold, and P. J. Huggins. The photodissociation of co in circumstellar envelopes. *ApJ ApJL The Astrophysical Journal*, 328:797, 1988.
- [26] C. Brinch and M. R. Hogerheijde. Lime – a flexible, non-lte line excitation and radiation transfer method for millimeter and far-infrared wavelengths. *Astronomy & Astrophysics A&A*, 523, 2010.